

¹ A novel inf-sup-based volumetric constraint ratio and
² its implementation via mixed FE-meshfree formulation

³ Junchao Wu^{a,*}, Yingjie Chu^b, Yangtao Xu^a

^a Key Laboratory for Intelligent Infrastructure and Monitoring of Fujian Province, College
of Civil Engineering, Huaqiao University , Xiamen, Fujian, 361021, China

^b Fujian Key Laboratory of Digital Simulations for Coastal Civil Engineering, Department
of Civil Engineering, Xiamen University , Xiamen, Fujian, 361005, China

⁴ **Abstract**

Numerical formulations for incompressible materials often suffer from volumetric locking, which reduces the accuracy of displacement solutions and introduces oscillations in the pressure field. A well-chosen constraint ratio can mitigate this issue, but traditional approaches lack a theoretical foundation based on the inf-sup (or LBB) condition, which is essential for the stability of mixed formulations. This paper introduces a novel optimal constraint ratio derived from the inf-sup condition to address volumetric locking. The inf-sup test, a numerical tool for verifying the inf-sup condition, is reaffirmed to be equivalent to the inf-sup condition through a variational approach. By incorporating a complete polynomial space whose dimension matches the number of displacement degrees of freedom (DOFs), a new inf-sup value estimator is developed, explicitly considering the constraint ratio. For a given number of displacement DOFs, when the pressure DOFs of a numerical formulation remain below a stabilized number that falls into the optimal constraint ratio range, this numerical formulation actually satisfies the inf-sup condition. To implement the optimal constraint ratio, a mixed finite element and meshfree formulation is proposed, where displacements are discretized using traditional finite element approximations, and pressures are approximated via the reproducing kernel meshfree method. Leveraging the globally smooth reproducing kernel shape functions, the constraint ratio can be flexibly adjusted to meet the inf-sup condition without the limit of element. For computational efficiency and ease of implementation, pressure nodes are placed on selected displacement nodes to maintain the optimal constraint ratio. Inf-sup tests and a series of 2D and 3D incompressible elasticity examples validate the proposed constraint ratio, demonstrating its effectiveness in eliminating volumetric locking and enhancing the performance of mixed finite element and meshfree formulations.

⁵ **Keywords:** Optimal constraint ratio, Inf-sup condition estimator, Volumetric
⁶ locking, Mixd formulation, Reproducing kernel meshfree approximation

^{*}Corresponding author

Email address: jcwu@hqu.edu.cn (Junchao Wu)
Preprint submitted to Elsevier

April 14, 2025

7 **1. Introduction**

8 The volumetric constraint is a necessary condition in the numerical formulation
 9 of incompressible materials like rubber and hydrogel. Proper imposition of
 10 this constraint is crucial for obtaining better numerical solutions; insufficient or
 11 excessive constraints will reduce the accuracy and stability of the solution [1].
 12 The volumetric constraint ratio [2], denoted as r , is often used to measure the
 13 level of constraint. It is defined as the total degrees of freedom (DOFs) of dis-
 14 placement divided by the total DOFs of pressure. Ideally, the optimal constraint
 15 ratio should be consistent with its governing partial differential equations. For
 16 example, in the two-dimensional (2D) case, the optimal constraint ratio is 2,
 17 since there are two governing equations for displacement and one for pressure.
 18 When the constraint ratio is less than 2, the formulation suffers from volumetric
 19 locking, while a constraint ratio greater than 2 can cause a coarse solution for
 20 pressure. These observations have been summarized as follows[2]:

$$r = \frac{2n_u}{n_p}, \quad \begin{cases} r > 2 & \text{too few constraints} \\ r = 2 & \text{optimal} \\ r < 2 & \text{too many constraints} \\ r \leq 1 & \text{severe locking} \end{cases} \quad (1)$$

21 where n_u and n_p are the numbers of control nodes for displacement and pressure,
 22 respectively. Classifying the locked status via the constraint ratio is straight-
 23 forward but imprecise. For instance, the constraint ratio can remain 2 while
 24 the pressure is discretized using continuous shape functions identical to the
 25 displacement's approximation. However, volumetric locking still exists in this
 26 formulation [2].

27 The inf-sup condition, also known as the Ladyzhenskay–Babuška–Brezzi
 28 (LBB) condition [3, 4], is a more precise requirement for a locking-free for-
 29 mulation. This condition is based on the mixed formulation framework, and
 30 when the inf-sup condition is satisfied, both the accuracy and stability of the
 31 mixed-formulation can be ensured. However, verifying the inf-sup condition is
 32 non-trivial. An eigenvalue problem namely inf-sup test can be used to check
 33 this condition numerically [5, 6, 7, 8]. Analytically, Brezzi and Fortin proposed
 34 a two-level projection framework that always satisfies the inf-sup condition, al-
 35 lowing it to be checked by identifying whether the formulation is included in
 36 this framework. Both analytical and numerical methods to check the inf-sup
 37 condition are complex, and the relationship between the constraint ratio and
 38 the inf-sup condition remains unclear.

39 To address volumetric constraint issues, adjusting the constraint ratio to an
 40 appropriate level is commonly used and easily implemented. In traditional finite
 41 element methods (FEM), this adjustment is carried out based on elements since
 42 the DOFs are embedded in each element. Conventional FEM often exhibits
 43 an over-constrained status. Reducing the approximation order of pressure in
 44 mixed formulation can alleviate the constraint burden, such as with the well-
 45 known Q4P1 (4-node quadrilateral displacement element with 1-node piecewise

constant pressure element) and Q8P3. Globally, using continuous shape functions to link the local pressure DOFs in each element can also reduce the total number of pressure DOFs and increase the constraint ratio, such as with T6C3 (6-node triangular displacement element with 3-node continuous linear pressure element) and Q9C4 (Taylor–Hood element) [9]. These schemes belong to the mixed formulation framework and can also be implemented through a projection approach, where the pressure approximant is projected into a lower-dimensional space. Examples include selective integration methods [10, 11], B–bar or F–bar methods [12, 13, 14, 15], pressure projection methods [16, 17, 18, 19, 20], and enhanced strain method [21]. Meanwhile, conventional 3-node triangular elements arranged in a regular cross pattern can also reduce the dimension of the pressure space [22]. It should be noted that not all of these methods meet the inf–sup condition despite alleviating volumetric locking and producing a good displacement solution. Some methods, like Q4P1, show significant oscillation for the pressure solution, known as spurious pressure mode or checkerboard mode [22]. In such cases, additional stabilization approaches, such as variational multi-scale stabilization (VMS) [23, 24, 25, 26, 27], Galerkin/least-squares (GLS) [28], or Streamline upwind/Petrov–Galerkin formulation (SUPG) [29, 30] are required to eliminate the oscillations in pressure.

Another class of FEM methods adjusts the constraint ratio by increasing the displacement DOFs. For instance, based on 3-node triangular elements, Arnold et al. [31, 32] used a cubic bubble function in each element to increase the displacement DOFs, known as the MINI element. It has been shown that this method belongs to the VMS framework [33], and its fulfillment of the inf–sup condition can be analytically evidenced using the two-level projection framework [7]. The Crouzeix–Raviart element [34] transfers the DOFs from the triangular vertices to edges, increasing the constraint ratio since, for triangular topology, the number of edges is greater than that of vertices. More details about FEM technology for volumetric constraint issues can be found in Refs. [2, 4, 35].

In the past two decades, various novel approximations equipped with globally smooth shape functions, such as moving least-squares approximation [36], reproducing kernel approximation [37, 38], radial basis functions [39, 40], maximum-entropy approximation [41], and NURBS approximation [42, 43], have been proposed. In these approaches, the approximant pressure evaluated by the derivatives of globally continuous shape functions also maintains a constraint ratio of 2 in 2D incompressible elasticity problems. However, the corresponding results still show lower accuracy caused by locking [44, 45]. Widely-used locking-free technologies for FEM are introduced in these approaches to enhance their performance. For example, Moutsanidis et al. [46, 47] employed selective integration and B–bar, F–bar methods for reproducing kernel particle methods. Wang et al. [48] applied selective integration schemes with bubble-stabilized functions to node-based smoothed particle FEM. Elguedj et al. [49] proposed the B–bar and F–bar NURBS formulations for linear and nonlinear incompressible elasticity. Chen et al. [50] adopted the pressure projection approach for reproducing kernel formulations for nearly-incompressible problems, which was later extended

to Stokes flow formulations by Goh et al. [51]. Bombarde et al. [52] developed a block-wise NURBS formulation for shell structures, eliminating locking via pressure projection. Casquero and Golestanian [53] proposed a NURBS-based continuous-assumed-strain element to alleviate volumetric locking. Most of these approximations offer better flexibility for arranging DOFs since their shape function constructions are no longer element-dependent. Huerta et al.[54] proposed a reproducing kernel approximation with divergence-free basis functions to avoid volumetric strain entirely , although this approach is unsuitable for compressible cases. Wu et al. [55] added extra displacement DOFs in FEM elements to resolve the locking issue, constructing local shape functions using generalized meshfree interpolation to maintain consistency. Vu-Huu et al. [56] employed different-order polygonal finite element shape functions to approximate displacement and pressure, embedding a bubble function in each element for stabilization.

This work proposes a more precise optimal volumetric constraint ratio and implements a locking-free mixed FE-meshfree formulation with this optimal constraint ratio. Firstly, the inf-sup condition is derived in a new form, showing that the inf-sup value equals to the lowest non-zero eigenvalue of dilatation stiffness in the context of variational analysis. Subsequently, involving a complete polynomial space with dimensions identical to displacement DOFs, the number of non-zero eigenvalues can be analytically calculated, and a new estimator considering the constraint ratio is established. From this estimator, the optimal constraint ratio is defined with a stabilized number of pressure nodes. If the constraint ratio exceeds the locking ratio, the formulation will show severe locking. When the constraint ratio is lower than the optimal ratio, the formulation achieves satisfactory results, and the inf-sup condition is fulfilled. This estimator provides a strong link between the inf-sup value and the pressure DOFs, making it possible to justify the locking status by counting the pressure nodes. Furthermore, a mixed FE-meshfree formulation is proposed to verify the optimal constraint ratio. In this mixed formulation, the displacement is approximated by traditional finite element methods, and the pressure is discretized by reproducing kernel meshfree approximation. With the aid of global RK shape functions, the pressure's DOFs can be adjusted arbitrarily without considering approximation order and numerical integration issues to maintaining the constraint ratio as optimal.

The remainder of this paper is organized as follows: Section 2 reviews the mixed formulation framework for incompressible elasticity problems. In Section 3, a novel estimator of the inf-sup value is developed, from which the optimal constraint ratio is obtained. Section 4 introduces the mixed FE-meshfree formulation and its corresponding nodal distribution schemes. Section 5 verifies the proposed optimal constraint ratio using a set of benchmark incompressible elasticity examples, studying error convergence and stability property for the mixed FE-meshfree approximation. Finally, the conclusions are presented in Section 6.

¹³⁶ **2. Mixed-formulation**

¹³⁷ *2.1. Nearly-incompressible elasticity*

¹³⁸ Consider a body $\Omega \in \mathbb{R}^{n_d}$ with boundary Γ in n_d -dimension, where Γ_t and
¹³⁹ Γ_g denote its natural boundary and essential boundary, respectively, such that
¹⁴⁰ $\Gamma_t \cup \Gamma_g = \Gamma$, $\Gamma_t \cap \Gamma_g = \emptyset$. The corresponding governing equations for the mixed
¹⁴¹ formulation are given by:

$$\begin{cases} \nabla \cdot \boldsymbol{\sigma} + \mathbf{b} = \mathbf{0} & \text{in } \Omega \\ \frac{p}{\kappa} + \nabla \cdot \mathbf{u} = 0 & \text{in } \Omega \\ \boldsymbol{\sigma} \cdot \mathbf{n} = \mathbf{t} & \text{on } \Gamma_t \\ \mathbf{u} = \mathbf{g} & \text{on } \Gamma_g \end{cases} \quad (2)$$

¹⁴² where \mathbf{b} denotes the prescribed body force in Ω . \mathbf{t}, \mathbf{g} are prescribed traction and
¹⁴³ displacement on natural and essential boundaries, respectively. \mathbf{u} and p , standing
¹⁴⁴ for displacement and hydrostatic pressure, respectively, are the variables of
¹⁴⁵ this problem. ∇ is the gradient tensor defined by $\nabla = \frac{\partial}{\partial x_i} \mathbf{e}_i$. $\boldsymbol{\sigma}$ denotes the
¹⁴⁶ stress tensor and has the following form:

$$\boldsymbol{\sigma}(\mathbf{u}, p) = p \mathbf{1} + 2\mu \nabla^d \mathbf{u} \quad (3)$$

¹⁴⁷ in which $\mathbf{1} = \delta_{ij} \mathbf{e}_i \otimes \mathbf{e}_j$ is the second-order identity tensor. $\nabla^d \mathbf{u}$ is the deviatoric
¹⁴⁸ gradient of \mathbf{u} and can be evaluated by:

$$\nabla^d \mathbf{u} = \frac{1}{2} (\mathbf{u} \nabla + \nabla \mathbf{u}) - \frac{1}{3} \nabla \cdot \mathbf{u} \quad (4)$$

¹⁴⁹ and κ, μ are the bulk modulus and shear modulus, respectively, and they can
¹⁵⁰ be represented by Young's modulus E and Poisson's ratio ν :

$$\kappa = \frac{E}{2(1-2\nu)}, \quad \mu = \frac{E}{3(1+\nu)} \quad (5)$$

¹⁵¹ In accordance with the Galerkin formulation, the weak form can be given
¹⁵² by: Find $\mathbf{u} \in V, p \in Q$, such that

$$\begin{cases} a(\mathbf{v}, \mathbf{u}) + b(\mathbf{v}, p) = f(\mathbf{v}) & \forall \mathbf{v} \in V \\ b(\mathbf{u}, q) + c(q, p) = 0 & \forall q \in Q \end{cases} \quad (6)$$

¹⁵³ with the spaces V, Q defined by:

$$V = \{\mathbf{v} \in H^1(\Omega)^2 \mid \mathbf{v} = \mathbf{g}, \text{ on } \Gamma_g\} \quad (7)$$

$$Q = \{q \in L^2(\Omega) \mid \int_{\Omega} q d\Omega = 0\} \quad (8)$$

155 where $a : V \times V \rightarrow \mathbb{R}$, $b : V \times Q \rightarrow \mathbb{R}$ and $c : Q \times Q \rightarrow \mathbb{R}$ are bilinear forms,
 156 and $f : V \rightarrow \mathbb{R}$ is the linear form. In elasticity problems, they are given by:

$$a(\mathbf{v}, \mathbf{u}) = \int_{\Omega} \nabla^d \mathbf{v} : \nabla^d \mathbf{u} d\Omega \quad (9)$$

$$b(\mathbf{v}, q) = \int_{\Omega} \nabla \cdot \mathbf{v} q d\Omega \quad (10)$$

$$c(q, p) = - \int_{\Omega} \frac{1}{3\kappa} q p d\Omega \quad (11)$$

$$f(\mathbf{v}) = \int_{\Gamma_t} \mathbf{v} \cdot \mathbf{t} d\Gamma + \int_{\Omega} \mathbf{v} \cdot \mathbf{b} d\Omega \quad (12)$$

157 *2.2. Ritz–Galerkin problem and volumetric locking*

158 In the mixed-formulation framework, the displacement and pressure can be
 159 discretized by different approximations. The approximant displacement \mathbf{u}_h and
 160 approximant pressure p_h can be expressed by:

$$\mathbf{u}_h(\mathbf{x}) = \sum_{I=1}^{n_u} N_I(\mathbf{x}) \mathbf{u}_I, \quad p_h(\mathbf{x}) = \sum_{K=1}^{n_p} \Psi_K(\mathbf{x}) p_K \quad (13)$$

161 leading these approximations into the weak form of Eq. (6) yields the following
 162 Ritz–Galerkin problems: Find $\mathbf{u}_h \in V_h$, $p_h \in Q_h$, such that

$$\begin{cases} a(\mathbf{v}_h, \mathbf{u}_h) + b(\mathbf{v}_h, p_h) = f(\mathbf{v}_h) & \forall \mathbf{v}_h \in V_h \\ b(\mathbf{u}_h, q_h) + c(q_h, p_h) = 0 & \forall q_h \in Q_h \end{cases} \quad (14)$$

163 For nearly incompressible material, the Poisson ratio approaches 0.5, and
 164 the bulk modulus κ will tend to infinity based on Eq. (5). Then, the bilinear
 165 form c in Eq. (11) tends to zero. And the weak form of Eq. (14) becomes an
 166 enforcement of the volumetric strain $\nabla \cdot \mathbf{u}_h$ to be zero using the Lagrangian
 167 multiplier method, where p_h is the Lagrangian multiplier.

168 Furthermore, from the second line of Eq. (14), we have:

$$b(\mathbf{u}_h, q_h) + c(q_h, p_h) = (q_h, \nabla \cdot \mathbf{u}_h) - (q_h, \frac{1}{3\kappa} p_h) = 0, \quad \forall q_h \in Q_h \quad (15)$$

169 or

$$(q_h, 3\kappa \nabla \cdot \mathbf{u}_h - p_h) = 0, \quad \forall q_h \in Q_h \quad (16)$$

170 where (\bullet, \bullet) is the inner product operator evaluated by:

$$(q, p) := \int_{\Omega} q p d\Omega \quad (17)$$

171 Obviously, in Eq. (16), p_h is the orthogonal projection of $3\kappa \nabla \cdot \mathbf{u}_h$ with respect
 172 to the space Q_h [1], and, for further development, we use the nabla notation

¹⁷³ with an upper tilde to denote the projection operator, i.e., $p_h = \tilde{\nabla} \cdot \mathbf{u}_h$. In this
¹⁷⁴ circumstance, the bilinear form b in the first line of Eq. (14) becomes:

$$\begin{aligned} b(\mathbf{v}_h, p_h) &= \underbrace{(\nabla \cdot \mathbf{v}_h - \tilde{\nabla} \cdot \mathbf{v}_h, p_h)}_0 + (\tilde{\nabla} \cdot \mathbf{v}_h, \underbrace{p_h}_{3\kappa \tilde{\nabla} \cdot \mathbf{u}_h}) \\ &= (\tilde{\nabla} \cdot \mathbf{v}_h, 3\kappa \tilde{\nabla} \cdot \mathbf{u}_h) \\ &= \tilde{a}(\mathbf{v}_h, \mathbf{u}_h) \end{aligned} \quad (18)$$

¹⁷⁵ where the bilinear form $\tilde{a} : V_h \times V_h \rightarrow \mathbb{R}$ is defined by:

$$\tilde{a}(\mathbf{v}_h, \mathbf{u}_h) = \int_{\Omega} 3\kappa \tilde{\nabla} \cdot \mathbf{v}_h \tilde{\nabla} \cdot \mathbf{u}_h d\Omega \quad (19)$$

¹⁷⁶ Accordingly, the problem of Eq. (14) becomes a one-variable form: Find
¹⁷⁷ $\mathbf{u}_h \in V_h$, such that

$$a(\mathbf{v}_h, \mathbf{u}_h) + \tilde{a}(\mathbf{v}_h, \mathbf{u}_h) = f(\mathbf{v}_h), \quad \forall \mathbf{v}_h \in V_h \quad (20)$$

¹⁷⁸ As $\kappa \rightarrow \infty$, Eq. (20) can be regarded as an enforcement of volumetric strain
¹⁷⁹ using the penalty method, where \tilde{a} is the penalty term. However, it should
¹⁸⁰ be noted that, if the mixed-formulation wants to obtain a satisfactory result,
¹⁸¹ this orthogonal projection must be surjective [57]. In the case where it is not
¹⁸² surjective, for a given $p_h \in Q_h$, it may not be possible to find a $\mathbf{u}_h \in V_h$ such that
¹⁸³ $p_h = 3\kappa \tilde{\nabla} \cdot \mathbf{u}_h$. This will lead to a much smaller displacement than expected and
¹⁸⁴ an oscillated pressure result. This phenomenon is called volumetric locking.

¹⁸⁵ 3. Optimal volumetric constraint ratio

¹⁸⁶ 3.1. Inf-sup condition and its eigenvalue problem

¹⁸⁷ To ensure the surjectivity of orthogonal projection and satisfactory results,
¹⁸⁸ the approximations of Eq.(7) should satisfy the inf-sup condition, also known
¹⁸⁹ as the Ladyzhenskaya–Babuška–Brezzi condition [4]:

$$\inf_{q_h \in Q_h} \sup_{\mathbf{v}_h \in V_h} \frac{|b(q_h, \mathbf{v}_h)|}{\|q_h\|_Q \|\mathbf{v}_h\|_V} \geq \beta > 0 \quad (21)$$

¹⁹⁰ in which β , namely the inf-sup value, is a constant independent of the char-
¹⁹¹ acterized element size h . The norms $\|\bullet\|_V$ and $\|\bullet\|_Q$ can be flexibly defined
¹⁹² by:

$$\|\mathbf{v}\|_V^2 := \int_{\Omega} \nabla^d \mathbf{v} : \nabla^d \mathbf{v} d\Omega \quad (22)$$

$$\|q\|_Q^2 := \int_{\Omega} \frac{1}{3\kappa} q^2 d\Omega \quad (23)$$

¹⁹³ To establish the relationship between the inf-sup condition and the con-
¹⁹⁴ straint ratio, the inf-sup condition is firstly transformed by the following Lemma
¹⁹⁵ 1:

196 **Lemma 1.** Suppose $\mathcal{P}_h : V_h \rightarrow Q_h$ is the orthogonal projection operator of the
197 divergence operator $\mathcal{P} := 3\kappa \nabla \cdot$, i.e., $\mathcal{P}_h := 3\kappa \bar{\nabla} \cdot$ and satisfies Eq. (16). Then,
198 the inf-sup value can be estimated by:

$$\beta \leq \inf_{V'_h \subset V_h \setminus \ker \mathcal{P}_h} \sup_{\mathbf{v}_h \in V'_h} \frac{\|\mathcal{P}_h \mathbf{v}_h\|_Q}{\|\mathbf{v}_h\|_V} \quad (24)$$

199 in which $\ker \mathcal{P}_h \subset V_h$ is the kernel of \mathcal{P}_h defined by $\ker \mathcal{P}_h := \{\mathbf{v}_h \in V_h \mid \mathcal{P}_h \mathbf{v}_h =$
200 0.

201 PROOF. First, define the image space of \mathcal{P}_h as $\text{Im}\mathcal{P}_h := \{p_h \in Q_h \mid \exists \mathbf{v}_h \in$
202 $V_h, p_h = \mathcal{P}_h \mathbf{v}_h\}$. Since $\mathcal{P}_h \subset Q_h$, Eq. (21) can be rewritten as:

$$\begin{aligned} \beta &\leq \inf_{q_h \in Q_h} \sup_{\mathbf{v}_h \in V_h} \frac{|b(q_h, \mathbf{v}_h)|}{\|q_h\|_Q \|\mathbf{v}_h\|_V} = \inf_{q_h \in Q_h} \sup_{\mathbf{v}_h \in V_h} \frac{|(q_h, \frac{1}{3\kappa} \mathcal{P} \mathbf{v}_h)|}{\|q_h\|_Q \|\mathbf{v}_h\|_V} \\ &\leq \inf_{q_h \in \text{Im}\mathcal{P}_h} \sup_{\mathbf{v}_h \in V_h} \frac{|\frac{1}{3\kappa} (q_h, \mathcal{P}_h \mathbf{v}_h)|}{\|q_h\|_Q \|\mathbf{v}_h\|_V} \end{aligned} \quad (25)$$

203 For a given $q_h \in \text{Im}\mathcal{P}_h$, suppose a space $V'_h \subseteq V_h \setminus \ker \mathcal{P}_h$ defined by:

$$V'_h = \{\mathbf{v}_h \in V_h \mid \mathcal{P}_h \mathbf{v}_h = q_h\} \quad (26)$$

204 Since $\text{Im}\mathcal{P}_h \subset Q_h$, according to the Cauchy-Schwarz inequality, we have:

$$\left| \frac{1}{3\kappa} (q_h, \mathcal{P}_h \mathbf{v}_h) \right| \leq \|q_h\|_Q \|\mathcal{P}_h \mathbf{v}_h\|_Q \quad (27)$$

205 where this equality holds if and only if $q_h = \mathcal{P}_h \mathbf{v}_h$, i.e.,

$$\left| \frac{1}{3\kappa} (q_h, \mathcal{P}_h \mathbf{v}_h) \right| = \|q_h\|_Q \|\mathcal{P}_h \mathbf{v}_h\|_Q, \quad \forall \mathbf{v}_h \in V'_h \quad (28)$$

206 And the following relationship can be evidenced:

$$\sup_{\mathbf{v}_h \in V_h} \frac{|\frac{1}{3\kappa} (q_h, \mathcal{P}_h \mathbf{v}_h)|}{\|q_h\|_Q \|\mathbf{v}_h\|_V} = \sup_{\mathbf{v}_h \in V'_h} \frac{\|\mathcal{P}_h \mathbf{v}_h\|_Q}{\|\mathbf{v}_h\|_V}, \quad \forall q_h \in \text{Im}\mathcal{P}_h \quad (29)$$

207 Consequently, by combining Eqs. (25) and (29), Eq. (24) can be obtained.

208 **Remark 1.** With Lemma 1 and the norm definitions in Eqs. (22),(23), the
209 square of the inf-sup value can further be bounded by:

$$\beta^2 \leq \inf_{V'_h \subset V_h \setminus \ker \mathcal{P}_h} \sup_{\mathbf{v}_h \in V'_h} \frac{\|\mathcal{P}_h \mathbf{v}_h\|_Q^2}{\|\mathbf{v}_h\|_V^2} = \inf_{V'_h \subset V_h \setminus \ker \mathcal{P}_h} \sup_{\mathbf{v}_h \in V'_h} \frac{\tilde{a}(\mathbf{v}_h, \mathbf{v}_h)}{a(\mathbf{v}_h, \mathbf{v}_h)} \quad (30)$$

210 The left-hand side of the above equation is consistent with the minimum-maximum
211 principle [58] and again proves the equivalence with the traditional numerical
212 inf-sup test [5]. Since that, β^2 evaluates the non-zero general eigenvalue of \tilde{a}
213 and a in Eq. (20).

214 3.2. Inf-sup value estimator

215 Subsequently, the relationship between constraint ratio and the inf-sup condition is established by the following Theorem:

217 **Theorem 1.** Suppose that P_{n_u} is a polynomial space with n_u dimensions, and
218 V_{n_u} is the polynomial displacement space, $V_{n_u} = P_{n_u}^{n_d}$. The inf-sup value β can
219 further be bounded by:

$$\beta \leq \beta_s + O(h) \quad (31)$$

220 with

$$\beta_s = \inf_{V' \subset V_{n_u} \setminus \ker \mathcal{P}_h \mathcal{I}_h} \sup_{\mathbf{v} \in V'} \frac{\|\mathcal{P}\mathbf{v}\|_Q}{\|\mathbf{v}\|_V} \quad (32)$$

221 where \mathcal{I}_h is the interpolation operator of the finite element approximation, and
222 correspondingly, $O(h)$ is the remainder related to h .

223 PROOF. As the dimensions of V_h and V_{n_u} are identical, $\dim V_{n_u} = \dim V_h =$
224 $n_d \times n_u$. There exists a unique $\mathbf{v} \in V_{n_u}$ satisfying $\mathbf{v}_h = \mathcal{I}_h \mathbf{v}$. And the right side
225 of Eq. (24) becomes:

$$\inf_{V'_h \subset V_h \setminus \ker \mathcal{P}_h} \sup_{\mathbf{v}_h \in V'_h} \frac{\|\mathcal{P}_h \mathbf{v}_h\|_Q}{\|\mathbf{v}_h\|_V} = \inf_{V' \subset V_{n_u} \setminus \ker \mathcal{P}_h \mathcal{I}_h} \sup_{\mathbf{v} \in V'} \frac{\|\mathcal{P}_h \mathcal{I}_h \mathbf{v}\|_Q}{\|\mathcal{I}_h \mathbf{v}\|_V} \quad (33)$$

226 According to the triangular inequality, Cauchy-Schwarz inequality, and the
227 relationship of Eqs. (16), we have:

$$\begin{aligned} \|\mathcal{P}_h \mathcal{I}_h \mathbf{v}\|_Q &= \sup_{q_h \in Q_h} \frac{|\frac{1}{3\kappa}(q_h, \mathcal{P}_h \mathcal{I}_h \mathbf{v})|}{\|q_h\|_Q} = \sup_{q_h \in Q_h} \frac{|\frac{1}{3\kappa}(q_h, \mathcal{P} \mathcal{I}_h \mathbf{v})|}{\|q_h\|_Q} \\ &\leq \sup_{q_h \in Q_h} \frac{|\frac{1}{3\kappa}(q_h, \mathcal{P} \mathbf{v})| + |\frac{1}{3\kappa}(q_h, \mathcal{P} \mathbf{v} - \mathcal{P} \mathcal{I}_h \mathbf{v})|}{\|q_h\|_Q} \quad (34) \\ &\leq \|\mathcal{P} \mathbf{v}\|_Q + \|\mathcal{P}(\mathbf{v} - \mathcal{I}_h \mathbf{v})\|_Q \end{aligned}$$

228 Obviously, the second term on the right side of Eq. (34) is the interpolation
229 error, and can be evaluated by [59]:

$$\|\mathcal{P}(\mathbf{v} - \mathcal{I}_h \mathbf{v})\|_Q \leq Ch^k |\mathbf{v}|_{H_k} \quad (35)$$

230 where, for a sufficiently smooth $\mathbf{v} \in V$, k equals to the interpolation order of
231 \mathcal{I}_h .

232 Further leading the relation $\|\mathcal{I}_h \mathbf{v}\|_V \geq C |\mathbf{v}|_{H_k}$ obtained from the closed
233 graph theorem [33] and considering Eqs. (34)-(35), the right-hand side of Eq.
234 (33) can be represented as:

$$\inf_{V' \subset V_{n_u} \setminus \ker \mathcal{P}_h \mathcal{I}_h} \sup_{\mathbf{v} \in V'} \frac{\|\mathcal{P}_h \mathcal{I}_h \mathbf{v}\|_Q}{\|\mathcal{I}_h \mathbf{v}\|_V} \leq \inf_{V' \subset V_{n_u} \setminus \ker \mathcal{P}_h \mathcal{I}_h} \sup_{\mathbf{v} \in V'} \frac{\|\mathcal{P} \mathbf{v}\|_Q}{\|\mathbf{v}\|_V} + O(h) \quad (36)$$

235 Substituting Eqs. (33),(36) into (24) finally proves Eqs. (31), (32).

236 As we can see in Eqs. (31) and (32), $\beta_s \geq 0$, the condition β_s being equal to
 237 0 or not determines whether the formulation can satisfy the inf-sup condition.
 238 If $\beta_s > 0$, as the mesh refines, the second term on the right-hand side of Eq.
 239 (31) will sharply reduce and can be ignored. In contrast, if $\beta_s = 0$, the second
 240 term will dominate, and the evaluation of β will be dependent to h . Therefore,
 241 the inf-sup condition is violated and numerical instability arises.

242 3.3. Polynomial-wise constraint counting

243 From the above subsection, we can know that whether β_s is zero or not
 244 determines whether the mixed-formulation can fulfill the inf-sup condition. Ac-
 245 cording to the expression of β_s in Eq. (32), as $\beta_s = 0$, the variable \mathbf{v} should
 246 belong to $\ker \mathcal{P}$, so the dimensions of the subspace in which $\beta_s \neq 0$, namely n_s ,
 247 can be evaluated by:

$$n_s = \dim(V_{n_u} \setminus \ker \mathcal{P}) \quad (37)$$

248 To further construct the relationship between the inf-sup value estimator in
 249 Eq. (31) and the constraint ratio $r = \frac{n_d \times n_u}{n_p}$, we should find the displacement
 250 and pressure DOFs in Eq. (31). With the definition of V_{n_u} , the number of
 251 displacement DOFs is easy to be evaluated by:

$$n_u = \dim V_{n_u} \quad (38)$$

252 With well-posed nodal distributions of displacement and pressure, the number
 253 of pressure DOFs has the following relationship:

$$n_p = \dim Q_h = \dim(\text{Im} \mathcal{P}_h) = \dim(V_{n_u} \setminus \ker \mathcal{P}_h \mathcal{I}_h) \quad (39)$$

254 Figure 1 illustrates how the relationship between n_s , n_p , and n_u influences
 255 the fulfillment of the inf-sup condition:

- 256 • As $n_p > n_s$, there must exist a subspace in space $V_{n_u} \setminus \ker \mathcal{P}_h \mathcal{I}_h$ belonging
 257 to $\ker \mathcal{P}$, resulting in $\beta_s = 0$, i.e., $V_{n_u} \setminus \ker \mathcal{P}_h \mathcal{I}_h \cap \ker \mathcal{P} \neq \emptyset$. At this cir-
 258 cumstance, the inf-sup condition cannot be satisfied, and the formulation
 259 will suffer from volumetric locking.
- 260 • As $n_p \leq n_s$, for well-posed nodal distributions, the space $V_{n_u} \setminus \ker \mathcal{P}_h \mathcal{I}_h$
 261 may be a subset of $V_{n_u} \setminus \ker \mathcal{P}$. Then, β_s will remain nonzero, and the
 262 formulation will be locking-free.

263 Summarily, the formulation can satisfy the inf-sup condition and alleviate
 264 volumetric locking if at least the number of pressure nodes n_p is less than n_s ,
 265 so we name n_s as the stabilized number of pressure nodes. At this moment,
 266 the volumetric constraint ratio should meet the following relation to ensure the
 267 inf-sup condition:

$$r_{opt} \geq \frac{n_d \times n_u}{n_s} \quad (40)$$

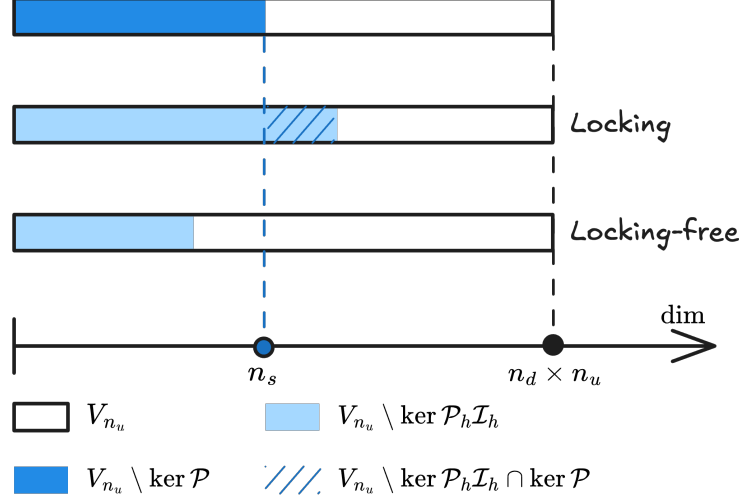


Figure 1: Illustration of estimator

268 **Remark 2.** Some uniform elements with special arrangements, like the union-
 269 jack element arrangement for 3-node triangular elements, can pass the inf-sup
 270 test [6], but their pressure DOFs number is greater than n_s . This is because the
 271 union-jack arrangement leads to a lower nonzero eigenvalue number of \tilde{a} and a
 272 in Eq. (20), and the corresponding nonzero eigenvalue number is less than or
 273 equal to the stabilized number n_s , satisfying Eq. (40). The similar cases about
 274 this special element arrangement are too few, so it is more straightforward to
 275 use the number of pressure nodes n_p to measure $\dim(V_{n_u} \setminus \ker \mathcal{P}_h \mathcal{I}_h)$.

276 **Remark 3.** It is obvious that the traditional optimal constraint ratio cannot
 277 fulfill this condition. However, not all formulations satisfying this condition
 278 can totally avoid volumetric locking. This is because $n_p \leq n_s$ is not equivalent
 279 to $V_{n_u} \setminus \ker \mathcal{P}_h \mathcal{I}_h \subset V_{n_u} \setminus \ker \mathcal{P}$. Fortunately, well-posed nodal distributions of
 280 displacement and pressure can ensure this, which will be evidenced by numerical
 281 examples in the subsequent sections.

282 3.4. Optimal volumetric constraint ratio

283 The fulfillment of the inf-sup condition should require the number of pres-
 284 sure nodes n_p to be lower than the stabilized number n_s , and now, we will
 285 demonstrate how to determine n_s for a specific number of displacement DOFs.

286 In the 2D case, for instance, we first consider the linear polynomial displace-
 287 ment space V_3 that is given by:

$$288 V_3 = \text{span} \left\{ \begin{pmatrix} 1 \\ 0 \end{pmatrix}, \begin{pmatrix} 0 \\ 1 \end{pmatrix}, \begin{pmatrix} x \\ 0 \end{pmatrix}, \begin{pmatrix} 0 \\ x \end{pmatrix}, \begin{pmatrix} y \\ 0 \end{pmatrix}, \begin{pmatrix} 0 \\ y \end{pmatrix} \right\} \quad (41)$$

²⁸⁸ or rearranged as follows,

$$V_3 = \text{span} \left\{ \underbrace{\left(\begin{array}{c} 1 \\ 0 \end{array} \right), \left(\begin{array}{c} 0 \\ 1 \end{array} \right), \left(\begin{array}{c} y \\ 0 \end{array} \right), \left(\begin{array}{c} 0 \\ x \end{array} \right), \left(\begin{array}{c} x \\ -y \end{array} \right)}_{\ker \mathcal{P}}, \underbrace{\left(\begin{array}{c} x \\ y \end{array} \right)}_{V_3 \setminus \ker \mathcal{P}} \right\} \quad (42)$$

²⁸⁹ It can be counted that, for $n_u = 3$, $n_s = 1$. Following the path, the displacement
²⁹⁰ space with a quadratic polynomial base, namely V_6 , can be stated as:

$$V_6 = \text{span} \left\{ \underbrace{\left(\begin{array}{c} 1 \\ 0 \end{array} \right), \left(\begin{array}{c} 0 \\ 1 \end{array} \right), \left(\begin{array}{c} y \\ 0 \end{array} \right), \left(\begin{array}{c} 0 \\ x \end{array} \right), \left(\begin{array}{c} x \\ -y \end{array} \right), \left(\begin{array}{c} x^2 \\ -2xy \end{array} \right), \left(\begin{array}{c} y^2 \\ 0 \end{array} \right), \left(\begin{array}{c} 0 \\ x^2 \end{array} \right), \left(\begin{array}{c} -2xy \\ y^2 \end{array} \right)}_{\ker \mathcal{P}}, \underbrace{\left(\begin{array}{c} x \\ y \end{array} \right), \left(\begin{array}{c} x^2 \\ 2xy \end{array} \right), \left(\begin{array}{c} 2xy \\ y^2 \end{array} \right)}_{V_6 \setminus \ker \mathcal{P}} \right\} \quad (43)$$

²⁹¹ In this circumstance, $n_s = 3$. As the order of the polynomial space increases, the
²⁹² optimal numbers of constraint DOFs for each order of the polynomial space are
²⁹³ listed in Table. 1, in which n denotes the order of space P_{n_u} . For the flexibility
²⁹⁴ of usage, the relation between n_u and n_s is summarized as follows:

$$n_s = \frac{n(n+1)}{2}, \quad n = \left\lfloor \frac{\sqrt{1+8n_u}-3}{2} \right\rfloor \quad (44)$$

Table 1: Relationship between the number of displacement nodes n_u and stabilized number of pressure nodes n_s

n	2D		3D	
	n_u	n_s	n_u	n_s
1	3	1	4	1
2	6	3	10	4
3	10	6	20	10
4	15	10	35	20
\vdots	\vdots	\vdots	\vdots	\vdots

²⁹⁵ For the 3D case, following the path in 2D, the linear polynomial space V_4 is
²⁹⁶ considered herein, and the arranged space of V_4 is listed as follows:

$$V_4 = \text{span} \left\{ \underbrace{\left(\begin{array}{c} 1 \\ 0 \\ 0 \end{array} \right), \left(\begin{array}{c} 0 \\ 1 \\ 0 \end{array} \right), \left(\begin{array}{c} 0 \\ 0 \\ 1 \end{array} \right), \left(\begin{array}{c} 0 \\ x \\ 0 \end{array} \right), \left(\begin{array}{c} 0 \\ 0 \\ x \end{array} \right), \left(\begin{array}{c} y \\ 0 \\ 0 \end{array} \right)}_{\ker \mathcal{P}}, \underbrace{\left(\begin{array}{c} 0 \\ 0 \\ y \end{array} \right), \left(\begin{array}{c} z \\ 0 \\ 0 \end{array} \right), \left(\begin{array}{c} 0 \\ z \\ 0 \end{array} \right), \left(\begin{array}{c} x \\ -y \\ 0 \end{array} \right), \left(\begin{array}{c} x \\ 0 \\ -z \end{array} \right), \left(\begin{array}{c} x \\ y \\ z \end{array} \right)}_{V_{n_u} \setminus \ker \mathcal{P}} \right\} \quad (45)$$

297 For brevity, the stabilized numbers for higher-order polynomial displacement
 298 spaces are directly listed in Table. 1, and it can be summarized that, for a given
 299 number of displacement DOFs, the stabilized number for pressure DOFs can be
 300 calculated as follows:

$$n_s = \frac{n(n+1)(n+2)}{6} \quad (46)$$

$$n = \left[\left(3n_u + \frac{1}{3} \sqrt{81n_u^2 - \frac{1}{3}} \right)^{\frac{1}{3}} + \frac{1}{3 \left(3n_u + \frac{1}{3} \sqrt{81n_u^2 - \frac{1}{3}} \right)^{\frac{1}{3}}} - 2 \right] \quad (47)$$

301 4. Mixed FE–meshfree formulation with optimal constraint ratio

302 In the proposed mixed-formulation, the displacement is approximated using
 303 3-node(Tri3), 6-node(Tri6) triangular elements and 4-node(Quad4), 8-node(Quad8)
 304 quadrilateral elements in 2D, 4-node(Tet4) tetrahedral element and 8-node(Hex8)
 305 hexahedral element in 3D [2]. In order to flexibly adjust to let the DOFs of
 306 pressure meet the optimal constraint, the reproducing kernel meshfree approxi-
 307 mation is involved to approximate pressure.

308 4.1. Reproducing kernel meshfree approximation

309 In accordance with the reproducing kernel approximation, the entire domain
 310 Ω , as shown in Figure 2, is discretized by n_p meshfree nodes, $\{\mathbf{x}_I\}_{I=1}^{n_p}$. The
 311 approximated pressure, namely p_h , can be expressed by the shape function Ψ_I
 312 and nodal coefficient p_I , yields:

$$p_h(\mathbf{x}) = \sum_{I=1}^{n_p} \Psi_I(\mathbf{x}) p_I \quad (48)$$

313 where, in the reproducing kernel approximation framework, the shape function
 314 Ψ_I is given by:

$$\Psi_I(\mathbf{x}) = \mathbf{c}(\mathbf{x}_I - \mathbf{x}) \mathbf{p}(\mathbf{x}_I - \mathbf{x}) \phi(\mathbf{x}_I - \mathbf{x}) \quad (49)$$

315 in which \mathbf{p} is the basis vector, for instance in the context of the 3D quadratic
 316 case, the basis vector takes the following form:

$$\mathbf{p}(\mathbf{x}) = \{1, x, y, z, x^2, y^2, z^2, xy, xz, yz\}^T \quad (50)$$

317 and ϕ stands for the kernel function. In this work, the traditional Cubic B-spline
 318 function with square or cube support is used as the kernel function:

$$\phi(\mathbf{x}_I - \mathbf{x}) = \phi(s_x)\phi(s_y)\phi(s_z), \quad s_i = \frac{\|\mathbf{x}_I - \mathbf{x}\|}{\bar{s}_{iI}} \quad (51)$$

319 with

$$\phi(s) = \frac{1}{3!} \begin{cases} (2-2s)^3 - 4(1-2s)^3 & s \leq \frac{1}{2} \\ (2-2s)^3 & \frac{1}{2} < s < 1 \\ 0 & s > 1 \end{cases} \quad (52)$$

³²⁰ where \bar{s}_{iI} 's are the support size towards the i -direction for the shape function
³²¹ Ψ_I . The correction function \mathbf{c} can be determined by the following so-called
³²² consistency condition:

$$\sum_{I=1}^{n_p} \Psi_I(\mathbf{x}) \mathbf{p}(\mathbf{x}_I) = \mathbf{p}(\mathbf{x}) \quad (53)$$

³²³ or equivalent shifted form:

$$\sum_{I=1}^{n_p} \Psi_I(\mathbf{x}) \mathbf{p}(\mathbf{x}_I - \mathbf{x}) = \mathbf{p}(\mathbf{0}) \quad (54)$$

³²⁴ Substituting Eq. 49 into Eq. (54) leads to:

$$\mathbf{c}(\mathbf{x}_I - \mathbf{x}) = \mathbf{A}^{-1}(\mathbf{x}_I - \mathbf{x}) \mathbf{p}(\mathbf{0}) \quad (55)$$

³²⁵ in which \mathbf{A} is namely the moment matrix evaluated by:

$$\mathbf{A}(\mathbf{x}_I - \mathbf{x}) = \sum_{I=1}^{n_p} \mathbf{p}(\mathbf{x}_I - \mathbf{x}) \mathbf{p}^T(\mathbf{x}_I - \mathbf{x}) \phi(\mathbf{x}_I - \mathbf{x}) \quad (56)$$

³²⁶ Taking Eq. (55) back to Eq. (49), the final form of the reproducing kernel shape
³²⁷ function can be obtained as:

$$\Psi_I(\mathbf{x}) = \mathbf{p}^T(\mathbf{0}) \mathbf{A}^{-1}(\mathbf{x}_I - \mathbf{x}) \phi(\mathbf{x}_I - \mathbf{x}) \quad (57)$$

³²⁸ As shown in Figure 2, reproducing kernel meshfree shape functions are glob-
³²⁹ ally smooth across the entire domain, using them to discretize the pressure field
³³⁰ allows the constraint ratio to be adjusted arbitrarily, without being limited by
³³¹ element topology. Moreover, when combined with finite element approxima-
³³² tions in Eq. 14, numerical integration can be conveniently performed within
³³³ each finite element ($\Omega'_C s$).

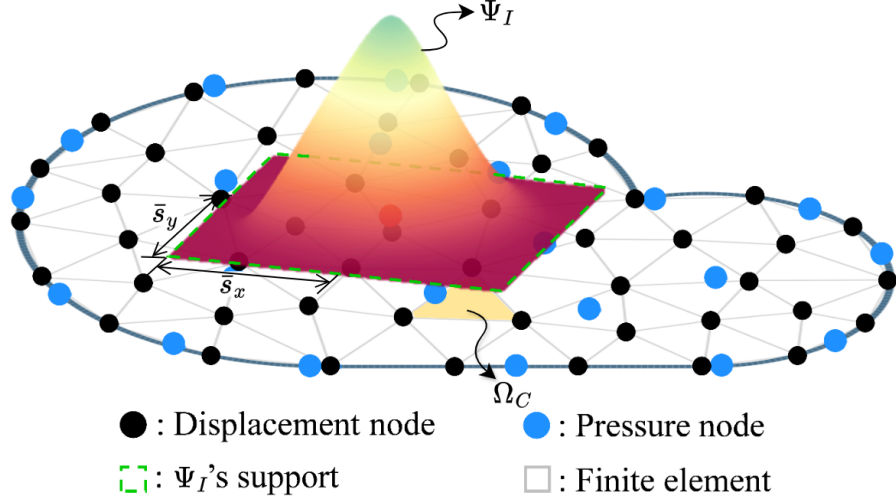


Figure 2: Illustration for reproducing kernel meshfree approximation

³³⁴ 4.2. Pressure node distributions with optimal constraint ratio

³³⁵ In this subsection, the 2D and 3D inf-sup tests [6] with the mixed FE-
³³⁶ meshfree formulations are employed to validate the proposed estimator of the
³³⁷ inf-sup value. The 2D test considers the square domain $\Omega = (0, 1) \otimes (0, 1)$ in
³³⁸ Figure 3a, where the displacement is discretized by Tri3 element, Quad4 element
³³⁹ with 4×4 , 8×8 , 16×16 and 32×32 elements, Tri6 element, Quad8 element
³⁴⁰ with 2×2 , 4×4 , 8×8 and 16×16 elements, respectively. The 3D test employs
³⁴¹ a cube domain $\Omega = (0, 1) \otimes (0, 1) \otimes (0, 1)$ in Figure 3b with 4×4 , 8×8 and
³⁴² 16×16 elements for the Tet4 element and Hex8 element. In order to avoid
³⁴³ the influence of interpolation error, uniform nodal distributions are used for
³⁴⁴ pressure discretizations.

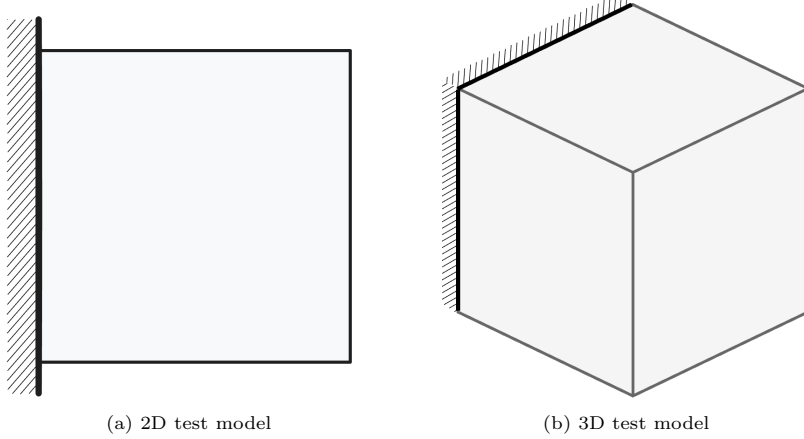


Figure 3: Illustration of inf-sup test

345 Figures 4–9 show the corresponding results, in which the red line stands for
 346 the value of β with respect to the number of pressure nodes n_p , and the vertical
 347 dashed line denotes the stabilized number n_s . The deeper color of the lines
 348 means mesh refinement. The results show that, no matter linear or quadratic
 349 elements, as n_p increases over n_s , the value of β sharply decreases, and then
 350 the inf-sup condition cannot be maintained. This result is consistent with the
 351 discussion in Section 3, and again verifies the effect of the proposed estimator.

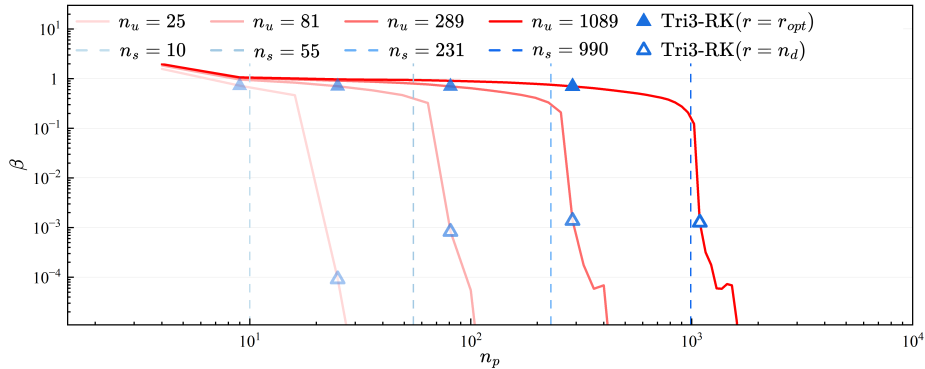


Figure 4: Inf-sup test for Tri3-RK

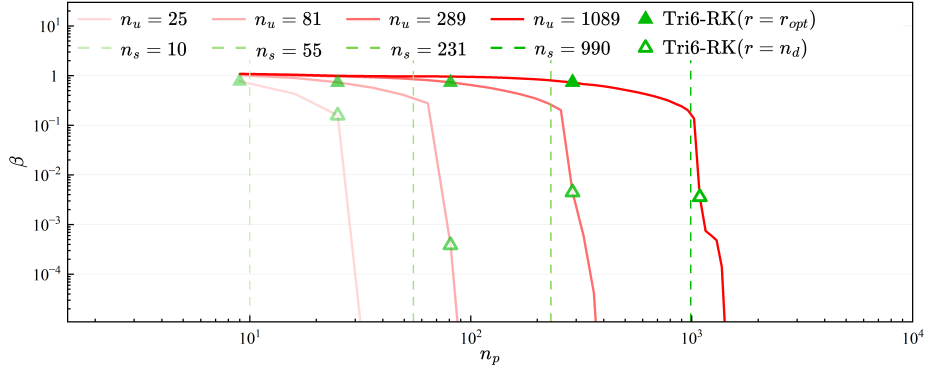


Figure 5: Inf-sup test for Tri6-RK

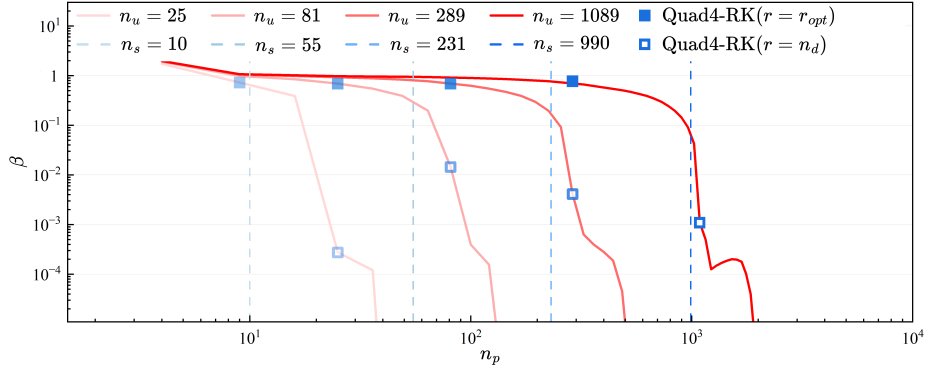


Figure 6: Inf-sup test for Quad4-RK

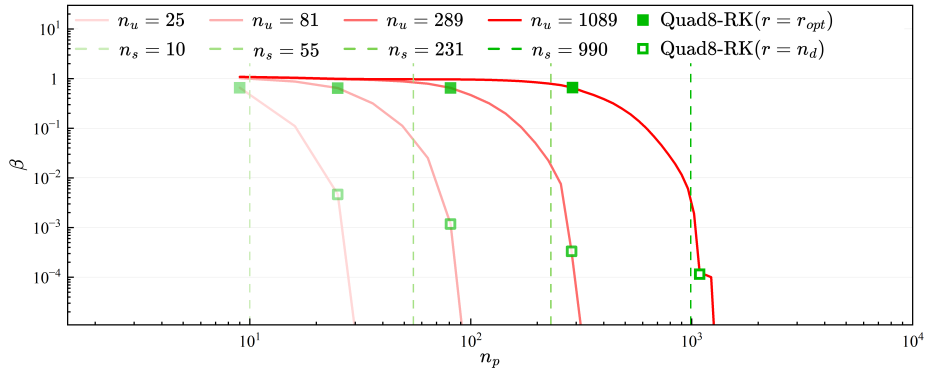


Figure 7: Inf-sup test for Quad8-RK

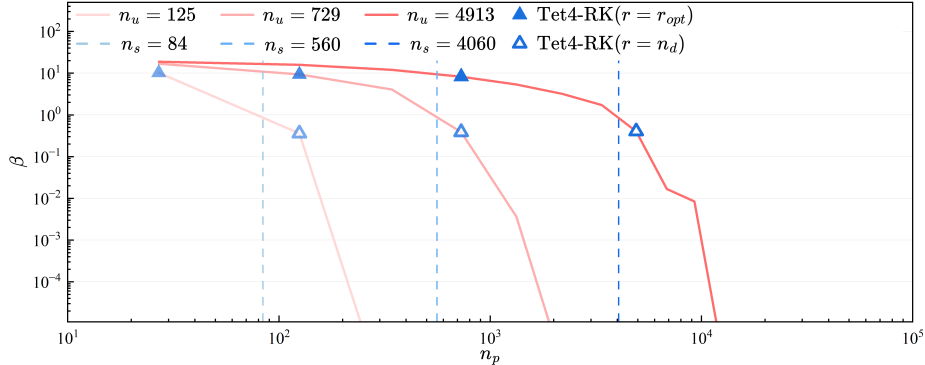


Figure 8: Inf-sup test for Tet4-RK

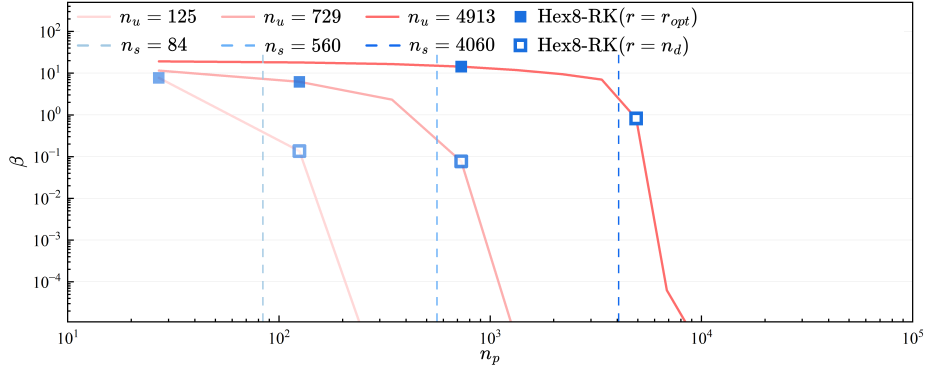


Figure 9: Inf-sup test for Hex8-RK

Moreover, the mixed formulation's results with the traditional optimal constraint ratio $r = n_d$ are listed in these figures as well, and β in this circumstance is already much smaller than those in the optimal range. Considering the results shown above, the easy programming and efficiency, the pressure nodes are chosen among the displacement nodes. The final schemes for linear and quadratic, 2D and 3D element discretizations are shown in Figure 10, in which all constraint ratios belong to the range of the optimal ratio. The corresponding inf-sup test results for these schemes are also marked in inf-sup test figure and show that, with mesh refinement, their β 's are always maintained at a non-negligible level.

5. Numerical examples

5.1. Cantilever beam problem

Consider the cantilever beam problem shown in Figure 11 with length $L = 48$, width $D = 12$, and the incompressible material parameters are employed with Young's modulus $E = 3 \times 10^6$, Poisson's ratio $\nu = 0.5 - 10^{-8}$. The left hand

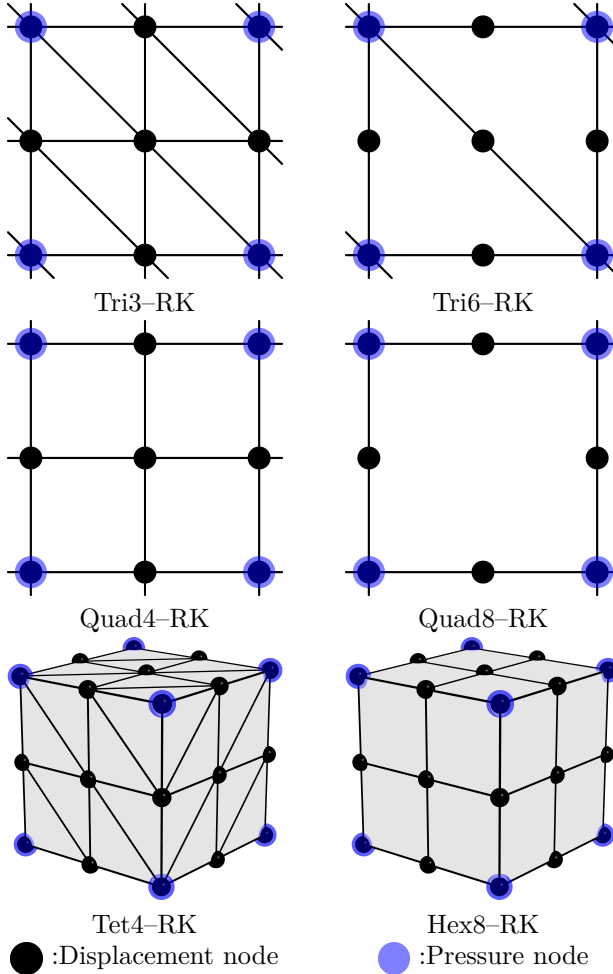


Figure 10: Nodal distribution schemes for mixed FE-meshfree formulations with $r = r_{opt}$

366 side is fixed and the right side subject to a concentrated force $P = 1000$. All
 367 the prescribed values in the boundary conditions are evaluated by the analytical
 368 solution that is given as follows [60]:

$$\begin{cases} u_x(\mathbf{x}) = -\frac{Py}{6EI} \left((6L - 3x)x + (2 + \bar{\nu})(y^2 - \frac{D^2}{4}) \right) \\ u_y(\mathbf{x}) = \frac{P}{6EI} \left(3\bar{\nu}y^2(L - x) + (4 + 5\bar{\nu})\frac{D^2x}{4} + (3L - x)x^2 \right) \end{cases} \quad (58)$$

³⁶⁹ where I is the beam's moment of inertia, \bar{E} and $\bar{\nu}$ are the material parameters
³⁷⁰ for plane strain hypothesis, they can be expressed by:

$$I = \frac{D^3}{12}, \quad \bar{E} = \frac{E}{1 - \nu^2}, \quad \bar{\nu} = \frac{\nu}{1 - \nu} \quad (59)$$

³⁷¹ And correspondingly, the stress components are evaluated by

$$\begin{cases} \sigma_{xx} = -\frac{P(L-x)y}{I} \\ \sigma_{yy} = 0 \\ \sigma_{xy} = \frac{P}{2I}\left(\frac{D^2}{4} - y^2\right) \end{cases} \quad (60)$$

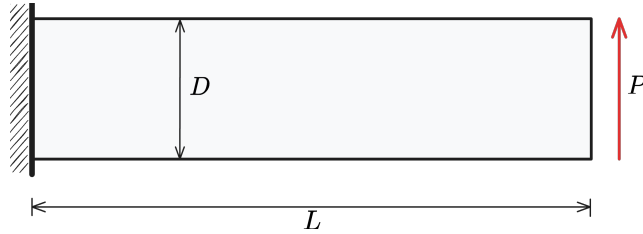


Figure 11: Illustration of cantilever beam problem

³⁷² In this problem, the Quad4 element with 16×4 , 32×8 , 64×16 , 128×32
³⁷³ grids, and Quad8 element with 8×2 , 16×4 , 32×8 , 64×16 grids are employed for
³⁷⁴ displacement discretization. The pressure is discretized by linear and quadratic
³⁷⁵ meshfree approximations with 1.5 and 2.5 characterized support sizes respec-
³⁷⁶ tively. The strain and pressure errors with respect to pressure nodes n_p are
³⁷⁷ displayed in Figure 12, where the vertical dashed lines stand for the stabilized
³⁷⁸ number n_s . The figure implies that the Quad8 shows better performance than
³⁷⁹ Quad4, since the Quad8's strain results are stable no matter the constraint ratio
³⁸⁰ is in the optimal range or not. And the Quad4's displacement errors increase
³⁸¹ as soon as $n_p > n_s$. However, both Quad4's and Quad8's pressure errors imme-
³⁸² diately increase while their constraint ratios are out of the optimal range, and
³⁸³ Quad8 still has better results than Quad4. Figure 13 shows the strain and pres-
³⁸⁴ sure error convergence comparisons for this cantilever beam problem, in which,
³⁸⁵ except Quad8-RK($r = n_d$) for strain error, all formulations with the traditional
³⁸⁶ constraint ratio of $r = n_d$ cannot ensure the optimal error convergence rates.
³⁸⁷ The proposed mixed formulations with $r = r_{opt}$ can maintain the optimal error
³⁸⁸ convergence ratio and show better accuracy.

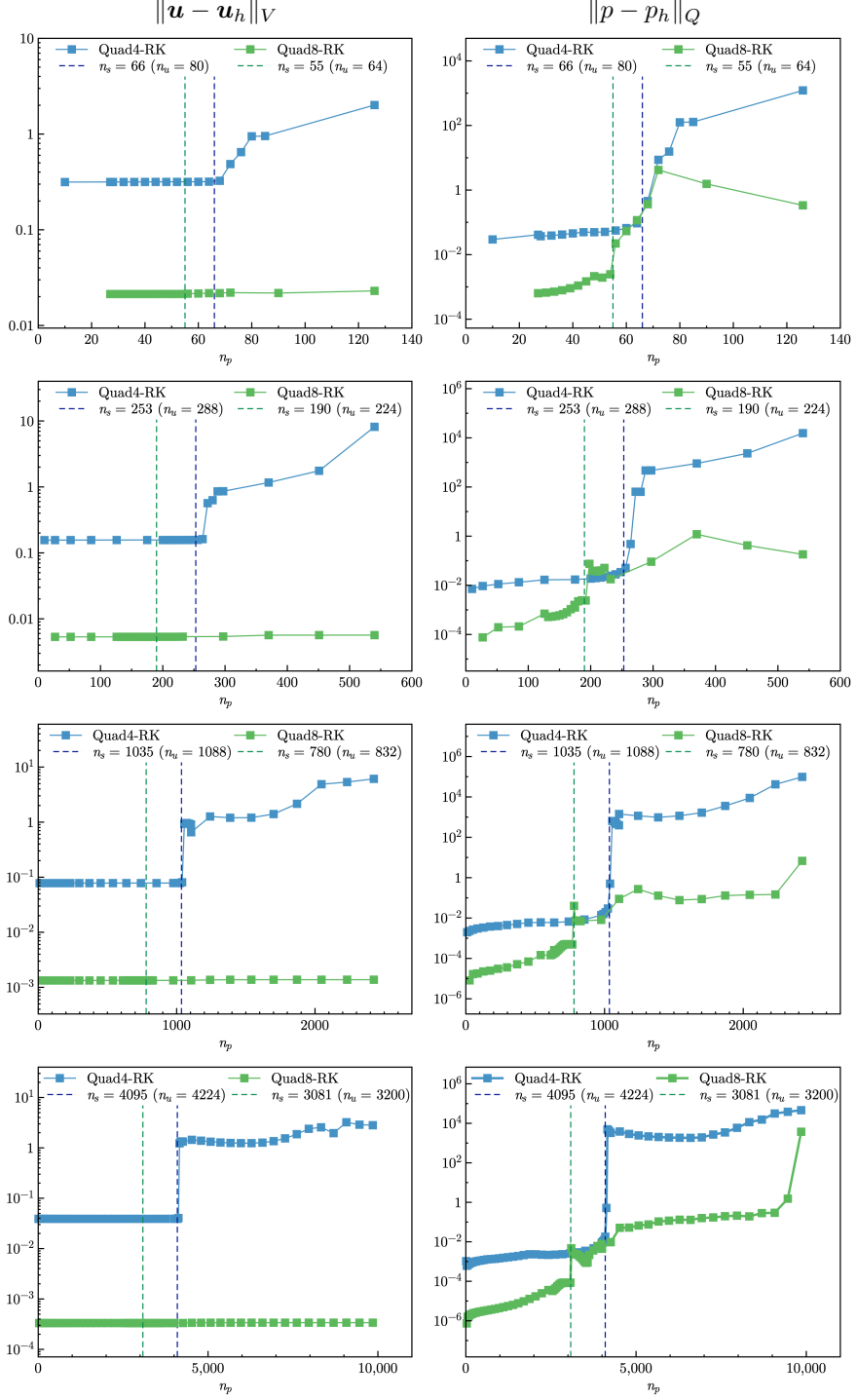


Figure 12: Strain and pressure errors vs. n_p for cantilever beam problem

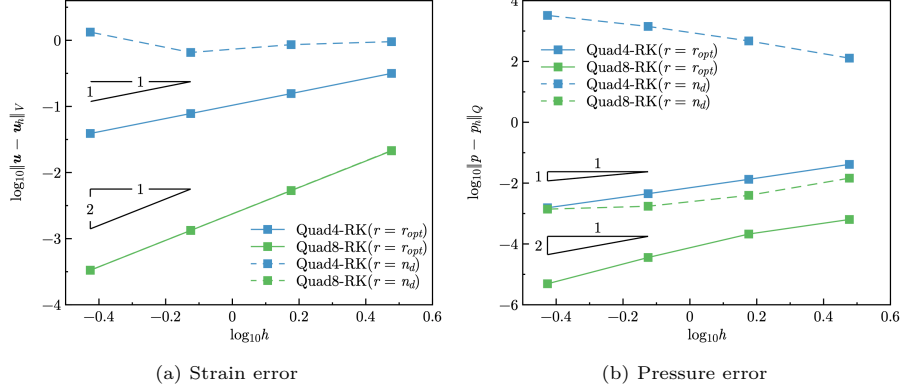


Figure 13: Error convergence study for cantilever beam problem

389 5.2. Plate with hole problem

Consider an infinite plate with a hole centered at the origin, as shown in Figure 14, and at the infinity towards the x -direction subjected to a uniform traction $T = 1000$. The geometric and material parameters for this problem are that the ratio of the hole $a = 1$, Young's modulus $E = 3 \times 10^6$, and Poisson's ratio $\nu = 0.5 - 10^{-8}$. The analytical solution of this problem refers to the Michell solution [60] as:

$$\begin{cases} u_x(\rho, \theta) = \frac{Ta}{8\mu} \left(\frac{\rho}{a}(k+1) \cos \theta - \frac{2a^3}{\rho^3} \cos 3\theta + \frac{2a}{\rho} ((1+k) \cos \theta + \cos 3\theta) \right) \\ u_y(\rho, \theta) = \frac{Ta}{8\mu} \left(\frac{\rho}{a}(k-3) \sin \theta - \frac{2a^3}{\rho^3} \sin 3\theta + \frac{2a}{\rho} ((1-k) \sin \theta + \sin 3\theta) \right) \end{cases} \quad (61)$$

396 in which $k = \frac{3-\nu}{1+\nu}$, $\mu = \frac{E}{2(1+\nu)}$. And the stress components are given by:

$$\begin{cases} \sigma_{xx} = T \left(1 - \frac{a^2}{\rho^2} \left(\frac{3}{2} \cos 2\theta + \cos 4\theta \right) + \frac{3a^4}{2\rho^4} \cos 4\theta \right) \\ \sigma_{yy} = -T \left(\frac{a^2}{\rho^2} \left(\frac{1}{2} \cos 2\theta - \cos 4\theta \right) + \frac{3a^4}{2\rho^4} \cos 4\theta \right) \\ \sigma_{xy} = -T \left(\frac{a^2}{\rho^2} \left(\frac{1}{2} \sin 2\theta + \sin 4\theta \right) - \frac{3a^4}{2\rho^4} \sin 4\theta \right) \end{cases} \quad (62)$$

According to the symmetry property of this problem, only a quarter model with length $b = 5$ is considered as shown in Figure 14. The displacement is discretized by 3-node and 6-node triangular elements with 81, 299, 1089, and 4225 nodes. The corresponding linear and quadratic meshfree formulations are employed for pressure discretization, and the characterized support sizes are chosen as 1.5 and 2.5, respectively. Figure 15 studies the relationship between strain, pressure errors, and n_p . Unlike the quadrilateral element case in Section 5.1, the quadratic Tri6-RK shows worse results while the constraint ratio is out

405 of the optimal range. And Tri3–RK exhibits less sensitivity in strain error than
 406 Tri6–RK, but its error is increasing while n_p goes up. Both Tri3–RK and Tri6–
 407 RK with constraint ratios under the optimal range perform acceptably. The
 408 corresponding error convergence study is presented in Figure 16, and only Tri3–
 409 RK with $r = 2$ shows a comparable result with the optimal one with $r = r_{opt}$.
 410 The other formulations with the traditional constraint ratio show lower accuracy
 411 and error convergence rates.

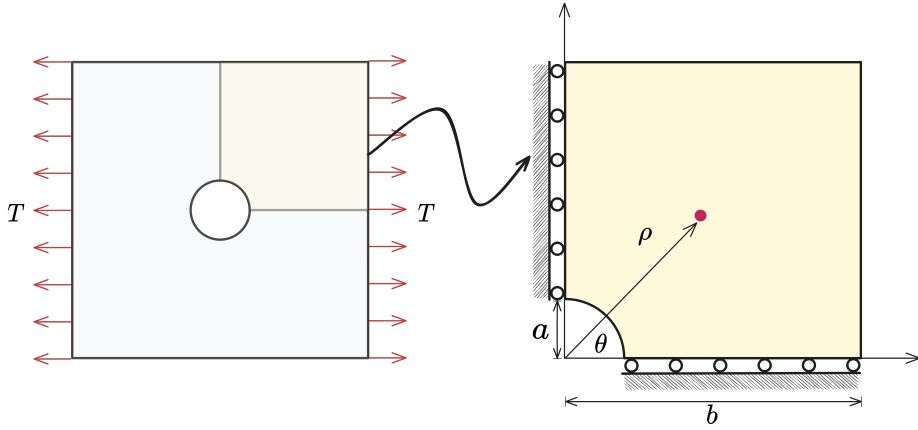


Figure 14: Illustration of plate with hole problem

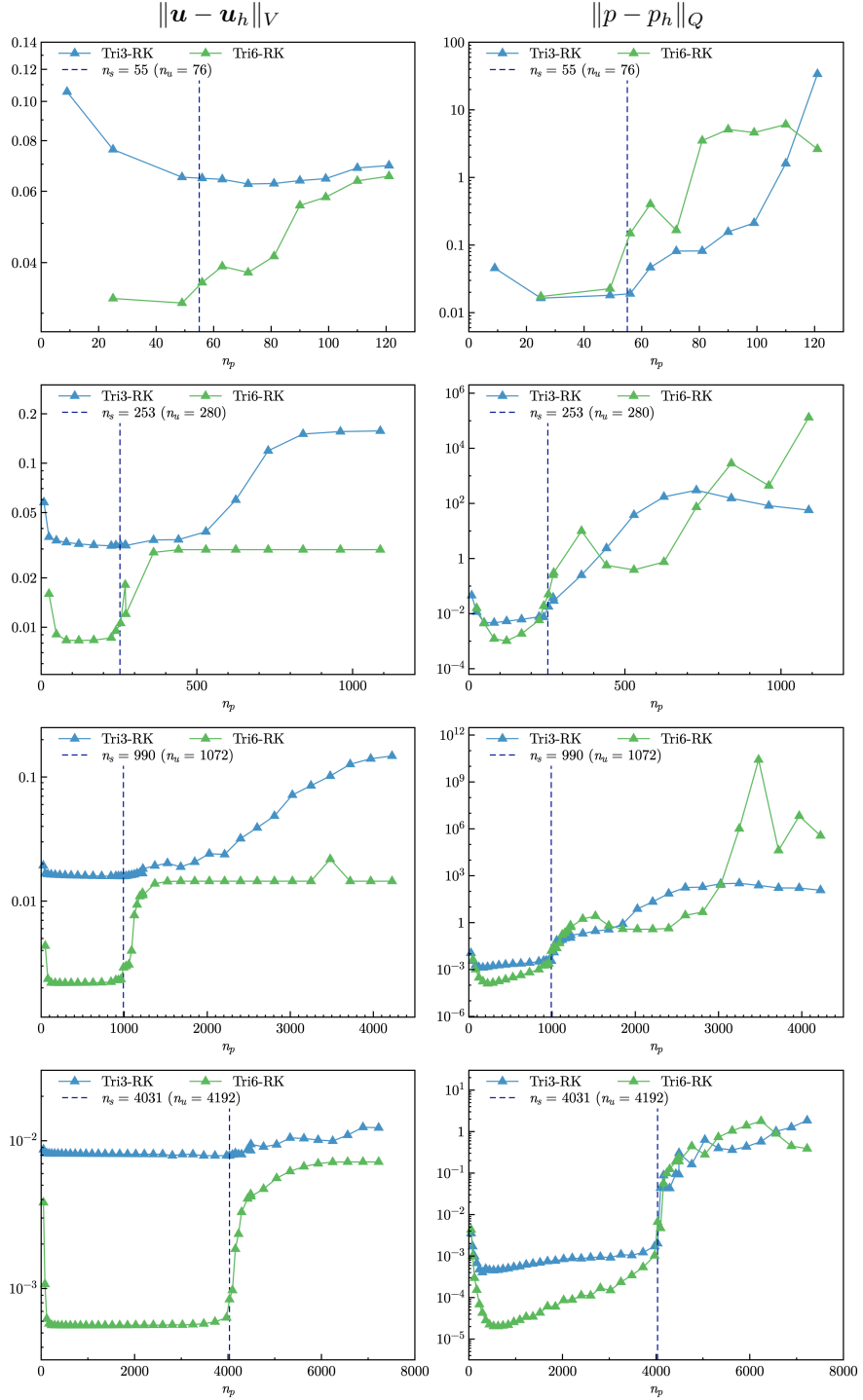


Figure 15: Strain and pressure errors vs. n_p for plate with hole problem

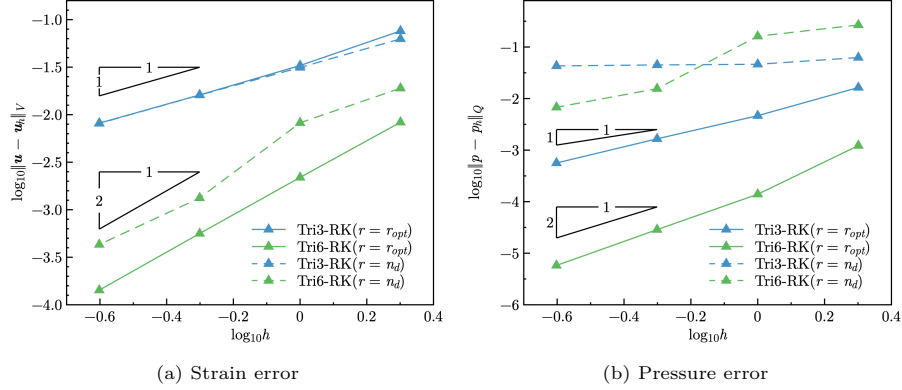


Figure 16: Error convergence study for plate with a hole problem

412 5.3. Cook membrane problem

The Cook membrane problem [12] is used herein for stability analysis of pressure. The geometry of this problem is shown in Figure 17, in which the left hand side is fixed and the right hand side subjects a concentrated force $P = 6.25$ in the y -direction. The material parameters are Young's modulus $E = 70.0$ and Poisson's ratio $\nu = 0.5 - 10^{-8}$.

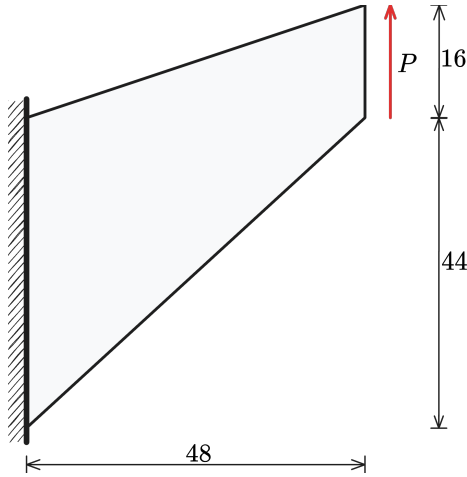


Figure 17: Illustration of Cook membrane problem

In this test, we focus on the pressure stability of 2D mixed FE–meshfree formulations. Figures 18–21 show the pressure contour plots for non-uniform Tri3–RK, Tri6–RK, Quad4–RK, and Quad8–RK formulations with $r = n_d$ and $r = r_{opt}$, respectively. The reproducing kernel meshfree approximations are employed for pressure discretization with characterized support sizes of 1.5 for the linear basis function and 2.5 for the quadratic basis function. The results

424 imply that the pressure contour plots with the optimal constraint ratio $r = r_{opt}$
 425 show a more stable and smooth pressure distribution compared to those with
 426 the traditional constraint ratio $r = n_d$.

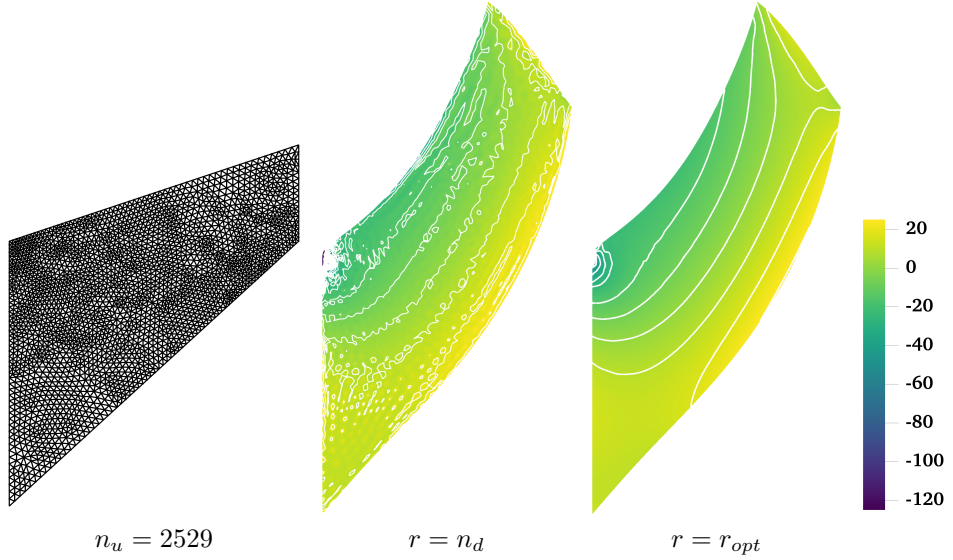


Figure 18: Pressure contour plots for Cook membrane problem using Tri3–RK

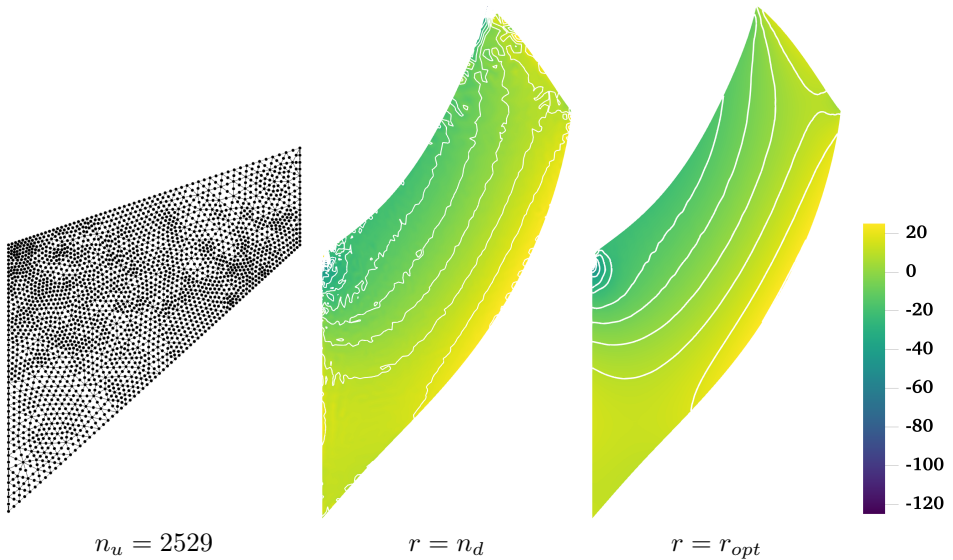


Figure 19: Comparison of pressure contour plots for Cook membrane problem using Tri6–RK

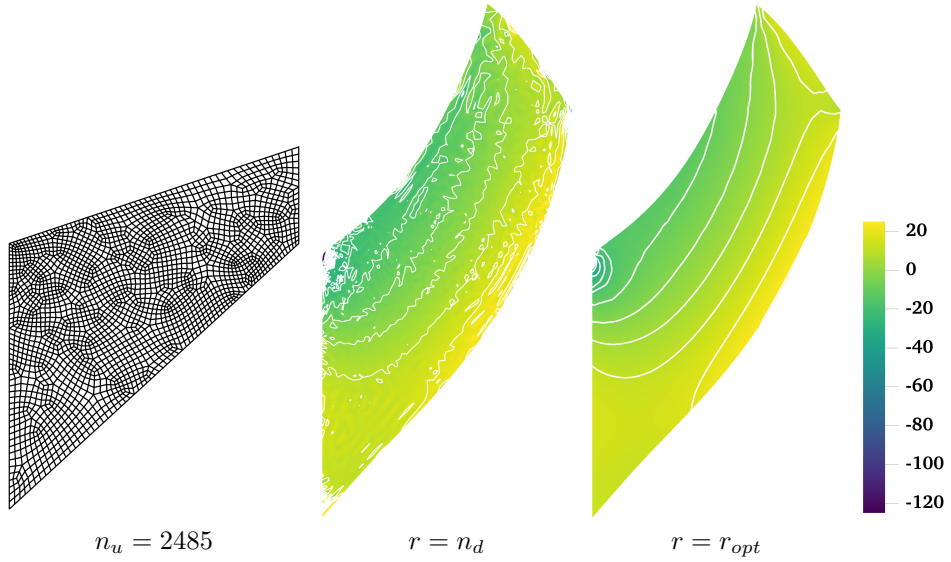


Figure 20: Comparison of pressure contour plots for Cook membrane problem using Quad4–RK

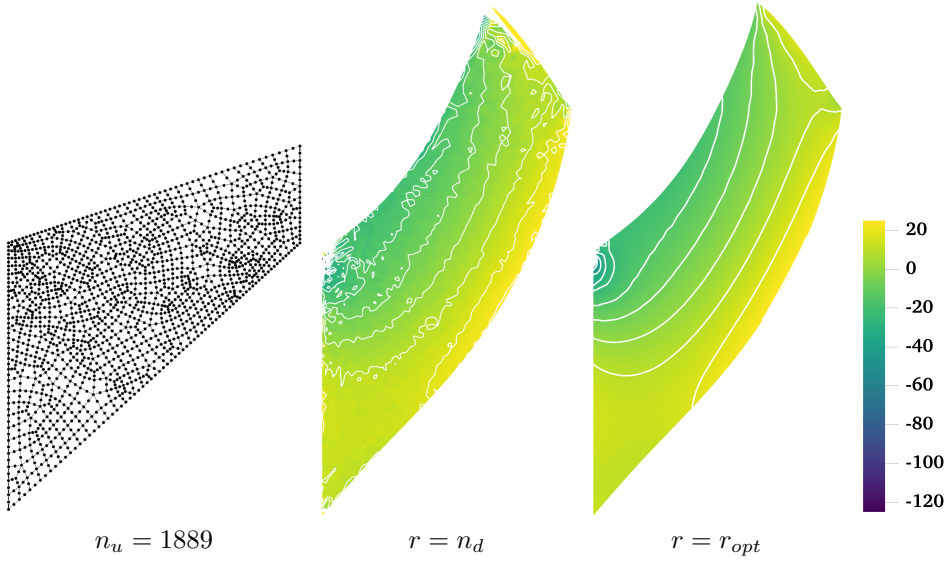


Figure 21: Comparison of pressure contour plots for Cook membrane problem using Quad8–RK

⁴²⁷ *5.4. Block under compression problem*

⁴²⁸ The incompressible block problem shown in Figure 22 is considered for test-
⁴²⁹ ing 3D mixed formulations. The block’s dimensions are $2L \times 2L \times L$, $L = 1$. At

430 the center of the top surface of the block is applied a pressure load $P = 80.0$
 431 with the area of $L \times L$. Due to the symmetry of this problem, only a quarter
 432 model is considered. The Young's modulus and Poisson's ratio are set as
 433 $E = 240.56839$ and $\nu = 0.5 - 10^{-8}$, respectively.

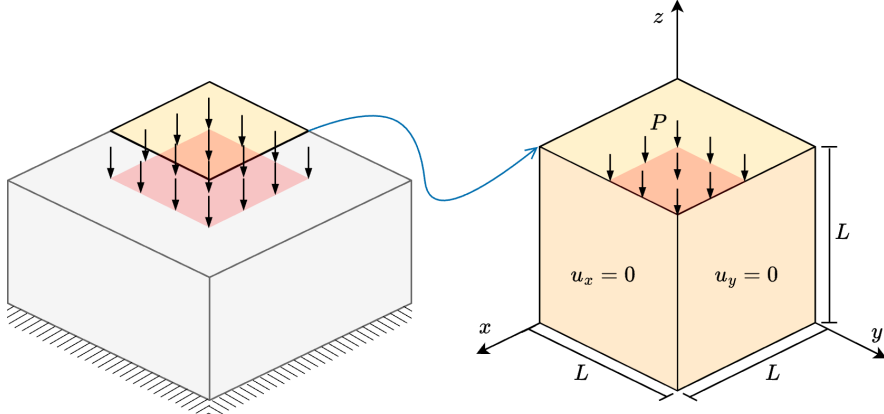


Figure 22: Illustration of block under compression problem

434 Figures study the pressure stability of 3D mixed FE-meshfree formulations,
 435 Tet4-RK and Hex8-RK, with non-uniform nodal distribution, while the pres-
 436 sure is discretized by linear meshfree approximations with a characterized sup-
 437 port size of 1.5. The corresponding results also show the well performance of
 438 the proposed optimal constraint ratio $r = r_{opt}$. The mixed formulations with
 439 the traditional constraint ratio $r = n_d$ show comparable displacement results,
 440 but exhibit significant pressure instability.

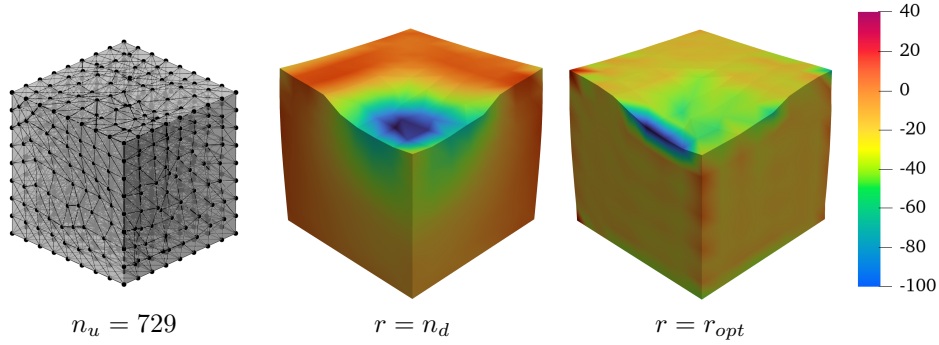


Figure 23: Comparison of pressure contour plots for block under compression problem using Tet4-RK

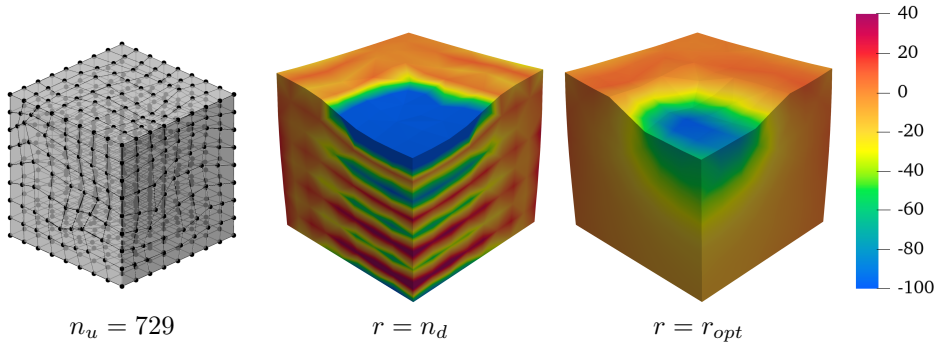


Figure 24: Comparison of pressure contour plots for block under compression problem using Hex8–RK

441 6. Conclusion

442 This paper proposes a novel optimal constraint ratio derived from the inf–sup
 443 condition to address volumetric locking. The optimal constraint ratio requires
 444 that, for a given number of displacement DOFs, the number of pressure DOFs
 445 should remain below a stabilized number determined by the proposed inf–sup
 446 value estimator. For well-posed nodal distribution, simply counting the dis-
 447 placement and pressure DOFs can determine whether the formulation satisfies
 448 the inf–sup condition. Compared to the traditional constraint ratio, the pro-
 449 posed ratio is theoretically grounded in the inf–sup condition and thus is more
 450 precise.

451 To implement this constraint ratio, a mixed finite element (FE) and meshfree
 452 formulation is developed. Displacements are discretized using 3-node and 6-node
 453 triangular elements, 4-node and 8-node quadrilateral elements in 2D, and 4-node
 454 tetrahedral and 8-node hexahedral elements in 3D. Correspondingly, linear and
 455 quadratic reproducing kernel meshfree approximations are used for pressure
 456 discretization. The reproducing kernel approximation equips globally smooth
 457 shape functions, allowing arbitrary pressure DOF placement without the limit
 458 of element.

459 Inf–sup tests for mixed FE–meshfree formulations with different constraint
 460 ratios verify the effectiveness of the proposed inf–sup value estimator. For effi-
 461 ciency and ease of implementation, the final nodal distribution scheme selects
 462 every other displacement node as a pressure node, ensuring the optimal con-
 463 straint ratio and satisfying the inf–sup condition.

464 A series of 2D and 3D incompressible elasticity examples demonstrate the
 465 effectiveness of the proposed mixed formulation. Results show that formulations
 466 with the optimal constraint ratio yield accurate displacement and pressure solu-
 467 tions. When the constraint ratio exceeds the optimal value, errors rise sharply
 468 to unacceptable levels, with the 8-node quadrilateral element being the only
 469 exception that maintains good displacement accuracy. Error convergence stud-
 470 ies and pressure contour plots further confirm that mixed formulations with

471 the optimal constraint ratio achieve optimal convergence rates and effectively
472 suppress pressure oscillations.

473 **Acknowledgment**

474 The support of this work by the National Natural Science Foundation of
475 China (12102138), the Natural Science Foundation of Fujian Province of China
476 (2023J01108) and the Fundamental Research Funds of Central Universities
477 (ZQN-1014) is gratefully acknowledged.

478 **References**

- 479 [1] F. Brezzi, M. Fortin, Mixed and Hybrid Finite Element Methods, Vol. 15 of
480 Springer Series in Computational Mathematics, Springer, New York, NY,
481 1991.
- 482 [2] T. J. Hughes, The Finite Element Method: Linear Static and Dynamic
483 Finite Element Analysis, Prentice Hall, New Jersey, 2000.
- 484 [3] I. Babuška, R. Narasimhan, The Babuška-Brezzi condition and the patch
485 test: An example, Computer Methods in Applied Mechanics and Engineering
486 140 (1-2) (1997) 183–199.
- 487 [4] K. J. Bathe, Finite Element Procedures, Prentice Hall, Englewood Cliffs,
488 New Jersey, 1996.
- 489 [5] D. S. Malkus, Eigenproblems associated with the discrete LBB condition for
490 incompressible finite elements, International Journal of Engineering Science
491 19 (10) (1981) 1299–1310.
- 492 [6] D. Chapelle, K. J. Bathe, The inf-sup test, Computers & Structures 47 (4)
493 (1993) 537–545.
- 494 [7] F. Brezzi, K. J. Bathe, Studies of finite element procedures the inf-sup
495 condition equivalent forms and applications.
- 496 [8] D. Gallistl, Rayleigh-Ritz approximation of the inf-sup constant for the
497 divergence, Mathematics of Computation 88 (315) (2019) 73–89.
- 498 [9] P. Hood, C. Taylor, Navier-Stokes equations using mixed interpolation,
499 Finite element methods in flow problems (1974) 121–132.
- 500 [10] D. S. Malkus, T. J. Hughes, Mixed finite element methods - Reduced and
501 selective integration techniques: A unification of concepts, Computer Meth-
502 ods in Applied Mechanics and Engineering 15 (1) (1978) 63–81.
- 503 [11] T. Shilt, R. Deshmukh, J. J. McNamara, P. J. O'Hara, Solution of nearly
504 incompressible field problems using a generalized finite element approach,
505 Computer Methods in Applied Mechanics and Engineering 368 (2020)
506 113165.

- 507 [12] J. C. Simo, M. S. Rifai, A class of mixed assumed strain methods and
 508 the method of incompatible modes, International Journal for Numerical
 509 Methods in Engineering 29 (8) (1990) 1595–1638.
- 510 [13] M. Broccardo, M. Micheloni, P. Krysl, Assumed-deformation gradient finite
 511 elements with nodal integration for nearly incompressible large deformation
 512 analysis, International Journal for Numerical Methods in Engineering 78 (9) (2009) 1113–1134.
- 514 [14] W. M. Coombs, T. J. Charlton, M. Cortis, C. E. Augarde, Overcoming vol-
 515 umetric locking in material point methods, Computer Methods in Applied
 516 Mechanics and Engineering 333 (2018) 1–21.
- 517 [15] S. Saloustros, M. Cervera, S. Kim, M. Chiumenti, Accurate and locking-free
 518 analysis of beams, plates and shells using solid elements, Computational
 519 Mechanics 67 (2021) 883–914.
- 520 [16] J. Simo, R. Taylor, K. Pister, Variational and projection methods for the
 521 volume constraint in finite deformation elasto-plasticity, Computer Meth-
 522 ods in Applied Mechanics and Engineering 51 (1-3) (1985) 177–208.
- 523 [17] C. R. Dohrmann, P. B. Bochev, A stabilized finite element method for the
 524 Stokes problem based on polynomial pressure projections, International
 525 Journal for Numerical Methods in Fluids 46 (2) (2004) 183–201.
- 526 [18] A. Valverde-González, J. Reinoso, B. Dortdivanlioglu, M. Paggi, Locking
 527 treatment of penalty-based gradient-enhanced damage formulation for fail-
 528 ure of compressible and nearly incompressible hyperelastic materials, Com-
 529 putational Mechanics 72 (2023) 635–662.
- 530 [19] B.-B. Xu, F. Peng, P. Wriggers, Stabilization-free virtual element method
 531 for finite strain applications, Computer Methods in Applied Mechanics and
 532 Engineering 417 (2023) 116555.
- 533 [20] F. S. Liguori, A. Madeo, S. Marfia, G. Garcea, E. Sacco, A stabilization-
 534 free hybrid virtual element formulation for the accurate analysis of 2D
 535 elasto-plastic problems, Computer Methods in Applied Mechanics and En-
 536 gineering 431 (2024) 117281.
- 537 [21] R. Alves de Sousa, R. Natal Jorge, R. Fontes Valente, J. César de Sá, A new
 538 volumetric and shear locking-free 3D enhanced strain element, Engineering
 539 Computations 20 (7) (2003) 896–925.
- 540 [22] K.-J. Bathe, The inf-sup condition and its evaluation for mixed finite ele-
 541 ment methods, Computers & Structures 79 (2) (2001) 243–252.
- 542 [23] T. J. R. Hughes, Multiscale phenomena: Green's functions, the Dirichlet-
 543 to-Neumann formulation, subgrid scale models, bubbles and the origins of
 544 stabilized methods, Computer Methods in Applied Mechanics and Engi-
 545 neering 127 (1) (1995) 387–401.

- 546 [24] R. Rossi, R. Zorrilla, R. Codina, A stabilised displacement-volumetric
 547 strain formulation for nearly incompressible and anisotropic materials,
 548 Computer Methods in Applied Mechanics and Engineering 377 (2021)
 549 113701.
- 550 [25] E. Karabelas, M. A. F. Gsell, G. Haase, G. Plank, C. M. Augustin, An
 551 accurate, robust, and efficient finite element framework with applications to
 552 anisotropic, nearly and fully incompressible elasticity, Computer Methods
 553 in Applied Mechanics and Engineering 394 (2022) 114887.
- 554 [26] R. Codina, I. Castañar, J. Baiges, Finite element approximation of stabi-
 555 lized mixed models in finite strain hyperelasticity involving displacements
 556 and stresses and/or pressure—An overview of alternatives, International
 557 Journal for Numerical Methods in Engineering (2024) e7540.
- 558 [27] L. Moreno, R. Wuechner, A. Larese, A mixed stabilized MPM formula-
 559 tion for incompressible hyperelastic materials using Variational Subgrid-
 560 Scales, Computer Methods in Applied Mechanics and Engineering 435
 561 (2025) 117621.
- 562 [28] T. J. R. Hughes, L. P. Franca, M. Balestra, A new finite element formu-
 563 lation for computational fluid dynamics: V. Circumventing the babuška-
 564 brezzi condition: A stable Petrov-Galerkin formulation of the stokes prob-
 565 lem accommodating equal-order interpolations, Computer Methods in Ap-
 566 plied Mechanics and Engineering 59 (1) (1986) 85–99.
- 567 [29] A. N. Brooks, T. J. R. Hughes, Streamline upwind/Petrov-Galerkin formu-
 568 lations for convection dominated flows with particular emphasis on the in-
 569 compressible Navier-Stokes equations, Computer Methods in Applied Me-
 570 chanics and Engineering 32 (1) (1982) 199–259.
- 571 [30] L. He, L. Jing, M. Feng, New stabilized mixed finite element methods for
 572 two-field poroelasticity with low permeability, Applied Mathematics and
 573 Computation 494 (2025) 129285.
- 574 [31] D. N. Arnold, F. Brezzi, M. Fortin, A stable finite element for the Stokes
 575 equations, CALCOLO 21 (4) (1984) 337–344.
- 576 [32] F. Auricchio, L. Beirão da Veiga, C. Lovadina, A. Reali, A stability study of
 577 some mixed finite elements for large deformation elasticity problems, Com-
 578 puter Methods in Applied Mechanics and Engineering 194 (9-11) (2005)
 579 1075–1092.
- 580 [33] A. Quarteroni, A. Valli, Numerical Approximation of Partial Differen-
 581 tial Equations, Springer Series in Computational Mathematics, Springer,
 582 Berlin, 1994.
- 583 [34] M. Crouzeix, P. Raviart, Conforming and nonconforming finite ele-
 584 ment methods for solving the stationary Stokes equations I, Revue

- 585 française d'automatique informatique recherche opérationnelle. Mathéma-
 586 tique 7 (R3) (1973) 33–75.
- 587 [35] U. Brink, E. Stein, On some mixed finite element methods for incompress-
 588 ible and nearly incompressible finite elasticity, Computational Mechanics
 589 19 (1) (1996) 105–119.
- 590 [36] T. Belytschko, Y. Y. Lu, L. Gu, Element-free Galerkin methods, Interna-
 591 tional Journal for Numerical Methods in Engineering 37 (2) (1994) 229–256.
- 592 [37] W. K. Liu, S. Jun, Y. F. Zhang, Reproducing kernel particle methods, Interna-
 593 tional Journal for Numerical Methods in Fluids 20 (8-9) (1995) 1081–
 594 1106.
- 595 [38] C. Rodriguez, T.-H. Huang, A variationally consistent reproducing ker-
 596 nel enhanced material point method and its applications to incompressible
 597 materials, Computational Mechanics (2023) 1–20.
- 598 [39] S. W. Chi, J. S. Chen, H. Y. Hu, A weighted collocation on the strong form
 599 with mixed radial basis approximations for incompressible linear elasticity,
 600 Computational Mechanics 53 (2) (2014) 309–324.
- 601 [40] L. Wang, Z. Qian, Y. Zhou, Y. Peng, A weighted meshfree collocation
 602 method for incompressible flows using radial basis functions, Journal of
 603 Computational Physics 401 (2020) 108964.
- 604 [41] A. Ortiz-Bernardin, M. Puso, N. Sukumar, Improved robustness for nearly-
 605 incompressible large deformation meshfree simulations on Delaunay tes-
 606 sellations, Computer Methods in Applied Mechanics and Engineering 293
 607 (2015) 348–374.
- 608 [42] T. J. Hughes, J. A. Cottrell, Y. Bazilevs, Isogeometric analysis: CAD,
 609 finite elements, NURBS, exact geometry and mesh refinement, Computer
 610 Methods in Applied Mechanics and Engineering 194 (39-41) (2005) 4135–
 611 4195.
- 612 [43] F. Auricchio, L. Beirão da Veiga, C. Lovadina, A. Reali, The importance
 613 of the exact satisfaction of the incompressibility constraint in nonlinear
 614 elasticity: Mixed FEMs versus NURBS-based approximations, Computer
 615 Methods in Applied Mechanics and Engineering 199 (5) (2010) 314–323.
- 616 [44] A. Huerta, S. Fernández-Méndez, Locking in the incompressible limit for
 617 the element-free Galerkin method, International Journal for Numerical
 618 Methods in Engineering 51 (11) (2001) 1361–1383.
- 619 [45] J. Dolbow, T. Belytschko, Volumetric locking in the element free Galerkin
 620 method, International Journal for Numerical Methods in Engineering 46 (6)
 621 (1999) 925–942.

- 622 [46] G. Moutsanidis, J. J. Koester, M. R. Tupek, J.-S. Chen, Y. Bazilevs, Treatment
 623 of near-incompressibility in meshfree and immersed-particle methods,
 624 Computational Particle Mechanics 7 (2) (2020) 309–327.
- 625 [47] G. Moutsanidis, W. Li, Y. Bazilevs, Reduced quadrature for FEM, IGA
 626 and meshfree methods, Computer Methods in Applied Mechanics and En-
 627 gineering 373 (2021) 113521.
- 628 [48] Z.-Y. Wang, Y.-F. Jin, Z.-Y. Yin, Y.-Z. Wang, Overcoming volumetric
 629 locking in stable node-based smoothed particle finite element method with
 630 cubic bubble function and selective integration, International Journal for
 631 Numerical Methods in Engineering 123 (24) (2022) 6148–6169.
- 632 [49] T. Elguedj, Y. Bazilevs, V. Calo, T. Hughes, B^- and F^- projection meth-
 633 ods for nearly incompressible linear and non-linear elasticity and plasticity
 634 using higher-order NURBS elements, Computer Methods in Applied Me-
 635 chanics and Engineering 197 (33-40) (2008) 2732–2762.
- 636 [50] J. S. Chen, S. Yoon, H. P. Wang, W. K. Liu, An improved reproducing
 637 kernel particle method for nearly incompressible finite elasticity, Computer
 638 Methods in Applied Mechanics and Engineering 181 (1) (2000) 117–145.
- 639 [51] C. M. Goh, P. M. F. Nielsen, M. P. Nash, A stabilised mixed mesh-
 640 free method for incompressible media: Application to linear elasticity and
 641 Stokes flow, Computer Methods in Applied Mechanics and Engineering 329
 642 (2018) 575–598.
- 643 [52] D. S. Bombarde, M. Agrawal, S. S. Gautam, A. Nandy, Hellinger–Reissner
 644 principle based stress–displacement formulation for three-dimensional iso-
 645 geometric analysis in linear elasticity, Computer Methods in Applied Me-
 646 chanics and Engineering 394 (2022) 114920.
- 647 [53] H. Casquero, M. Golestanian, Vanquishing volumetric locking in quadratic
 648 NURBS-based discretizations of nearly-incompressible linear elasticity:
 649 CAS elements, Computational Mechanics 73 (6) (2024) 1241–1252.
- 650 [54] A. Huerta, Y. Vidal, P. Villon, Pseudo-divergence-free element free
 651 Galerkin method for incompressible fluid flow, Computer Methods in Ap-
 652 plied Mechanics and Engineering 193 (12-14) (2004) 1119–1136.
- 653 [55] C. T. Wu, W. Hu, J. S. Chen, A meshfree-enriched finite element method
 654 for compressible and near-incompressible elasticity, International Journal
 655 for Numerical Methods in Engineering 90 (7) (2012) 882–914.
- 656 [56] T. Vu-Huu, C. Le-Thanh, H. Nguyen-Xuan, M. Abdel-Wahab, A high-
 657 order mixed polygonal finite element for incompressible Stokes flow analy-
 658 sis, Computer Methods in Applied Mechanics and Engineering 356 (2019)
 659 175–198.

- 660 [57] E. Stein, R. de Borst, T. J. R. Hughes (Eds.), Encyclopedia of Computational Mechanics, John Wiley, Chichester, West Sussex, 2004.
- 661
- 662 [58] I. Babuška, J. Osborn, Eigenvalue Problems, in: Handbook of Numerical Analysis, Vol. 2 of Finite Element Methods (Part 1), Elsevier, 1991, pp. 641–787.
- 663
- 664
- 665 [59] K. Yosida, Functional Analysis, 6th Edition, Classics in Mathematics, Springer-Verlag, Berlin Heidelberg, 1995.
- 666
- 667 [60] S. Timoshenko, J. Goodier, Theory of Elasticity, Engineering Mechanics Series, McGraw-Hill, 1969.
- 668